Biconical emission of spatially mode-locked patterns with wave-number ratio $\sqrt{2}$ in a ring cavity device

M. Le Berre, D. Leduc, E. Ressayre, and A. Tallet
Laboratoire de Photophysique Moléculaire du Centre National de la Recherche Scientifique, batiment 213, 91405 Orsay, France
(Received 18 January 1996; revised manuscript received 18 April 1996)

Biconical emission with wave-number ratio $\sqrt{2}$ is observed in the numerical simulations of the ring cavity with diffraction effects, on the defocusing side of the resonance. As the intensity of the plane-wave input beam increases, a sequence of stationary patterns is observed, and understood via a nonlinear analysis. The first pattern with (4-4) peaks is a bisquare resulting from a strong coupling between two quasiresonant sets of modes with wave numbers K and $\sqrt{2}K$. This pattern destabilizes at the onset of the drift bifurcation, into a new (4-4) pattern with a smaller wavelength, that splits into two twisted bisquares, with a 53° rotation angle ensuring the wave-vector locking, or the spatial periodicity of this (8-8) structure. [S1050-2947(96)09609-6]

PACS number(s): 42.65.−k, 42.55.−f

I. INTRODUCTION

The presence of several critical wave numbers $\{K,K',K''...\}$ near the onset of an instability was predicted to occur [1–5] in several optical devices, due to diffraction effects in the feedback loop. It should bias in favor of a multiconical emission of light with maxima of intensity in the far-field (spatial Fourier spectrum), distributed on several concentric rings with radii proportional to $K,K',K''...$. This effect was indeed observed [6], but not yet studied.

Here we analyze the patterns observed in the simulations of a passive ring cavity with a dispersive quasi-Kerr medium, illuminated by a *cw* red-shifted pump beam. On the defocusing side of the atomic resonance the values of the critical wave numbers are nearly equal to $\{K,\sqrt{2}K,\sqrt{3}K,2K...\}$. With a low-pass filter transparent to the first three cones, the biconical pattern spontaneously emerging from noise display patterns built up with the K and $\sqrt{2}K$ modes.

In another context, bicriticality *with* ''magic value'' was recently invoked by Müller [7] to be responsible for the formation of a new class of patterns with quasiperiodic order (the design is not periodic in any direction) called quasipatterns. He modelized such pattern formation by a pair of equations for two weakly coupled order parameters $\{u,u'\}$ having critical wave numbers $\{K,K'\}$, respectively, with $K'=\rho K$. For a suitable value of ρ, the structures obtained with coupling are simply the addition of two riveting patterns obtained without coupling. He illustrates the stabilization mechanism with two examples. He considers firstly the case of a model equation for u and u' leading to a square structure in the absence of coupling. With a quadratic interaction he obtained an eightfold quasipattern either for u, or for u', when $\rho=\sqrt{2\pm\sqrt{2}}$, with a spectrum composed by eight spots regularly distributed on a circle. Such a structure may be seen as two square patterns twisted by the angle $\pi/8$ relative to each other. Secondly, with another set of model equations leading to a hexagonal pattern in the absence of coupling, he obtained a twelvefold quasipattern with a weak coupling and $\rho=\sqrt{2\pm\sqrt{3}}$ or $\rho=\sqrt{2}$. The twelvefold orientational order results from two hexagonal patterns twisted by an angle $\pi/2$.

Our numerical simulations of the ring cavity display, near the onset of instability, a stable bisquare pattern with two sets of active orthogonal wave vectors $\{K,\sqrt{2}K\}$, that drastically changes the hexagonal order corresponding to the monoconical emission. Recall that hexagons are observed in the ring cavity when a single set of active modes is involved, i.e., either with the uniform field model which has a single critical wave number [8,9], or with our delay model when the second minimum is far away from the second, (on the focusing side of the resonance because $K'\gg K$, and on the defocusing side with a circular input beam removing the degeneracy between the conical emissions [2]). Thus the coupling mechanism between the set of vectors $\{K,\sqrt{2}K\}$, differs from the one considered by Müller.

In this paper we mainly describe the bisquare patterns obtained on a large domain above the threshold when the two sets of critical wave number K and $\sqrt{2}K$ become simultaneously active, i.e., with a plane-wave input beam and a tuned cavity. The patterns that spontaneously emerge from noise, or from a strong initial hexagonal modulation, definitely departs from the hexagonal order. It consists in two sets of (4-4) spots in quincunx in the far-field, called bisquare [with the definition of a $(n\text{-}m)$ pattern as having n and m bright spots on two concentric rings in the spectrum].

The linear analysis of the ring cavity equations with a plane-wave input is recalled in Sec. II. Section III displays the numerical and analytical study of the (4-4) patterns generated in a large domain of the critical parameter μ, from the threshold, $\mu=0$, up to $\mu=.75$, in the case of a plane-wave input beam. Above this value (8-8) and (8-12) patterns with periodic order are formed (Sec. IV). The case of a circular input beam is discussed in Sec. V.

II. MODEL EQUATIONS: LINEAR ANALYSIS

A. Delay model

The ring cavity equations under study are basically the Ikeda equations [10] for the electric field E at the cell entrance and the atomic energy ϕ, including diffraction in the free space of the cavity [1,2,11]

$$E(t+d,\vec{x})=E_0(\vec{x})+\rho\,\exp\left[i\,\frac{L}{2k}\,\nabla_T^2\right]E(t,\vec{x})$$
$$\times\exp[\alpha l(1+i\,\eta\Delta)\phi/2-i\,\eta\theta_{cav}], \quad (1a)$$

$$T_1\,\frac{d\phi}{dt}=-(\phi+1)-\frac{e^{\alpha l\phi}-1}{\alpha 1}\,|E|^2. \quad (1b)$$

The notations are those of Refs. [2, 11], E is the complex amplitude of the electric field, $\epsilon=1/2(Ee^{-i(\omega t-kz)}+\text{c.c.})$, scaled to the square root of the off-resonance saturation intensity, and $\phi=\int_0^l w(z)\,dz$ is the total energy stored by the atoms through the cell of length l [$w(z)$ is the population inversion in the medium]. $E_0(\vec{x})$ is the input amplitude of the cw laser at the cell entrance, d is the round trip time of the light inside the cavity, $\vec{x}$ is the transverse coordinate. Other parameters and symbols are: ρ is the mirror reflectivity, L the total effective diffraction length in the cavity (cell length l plus free-space diffraction path in the nonconfocal cavity), k the longitudinal wave vector, ∇_T^2 the transverse Laplacian, θ_{cav} the cavity mistuning, $\Delta=T_2|\omega_{ab}-\omega_L|$ where ω_{ab} is the atomic resonance frequency, and ω_L the cw laser beam frequency; αl is the off-resonance absorption coefficient of the medium, and $\eta=+1$ for the focusing case, -1 for the defocusing case.

This delay model was borne out in Ref. [2] with the criterium that the threshold characteristics of the linear analysis agree with those of a full set of Maxwell-Bloch equations. It was shown [11] that they are valid in the dispersive limit [12], for a good cavity, and when the diffraction path L inside the free space of the cavity is much larger than the cell length l. More precisely, the study was done for the following values of the parameters:

$$\alpha l=0.1, \quad \frac{\alpha l\Delta}{2}=4\pi, \quad (\Delta\approx 250), \quad \rho=0.95, \quad d=T_1 \quad (2)$$

that are still chosen in the present work.

The instability boundary which displays static multiconical emission, for a plane-wave input, was reported in Ref. [11]. It appears that biconical emission dealing with the near-axis cones is very different for a tuned cavity on both sides of the resonance, since the ratio of the first critical wave numbers is equal to 5.7 for the focusing case, while it is close to $\sqrt{2}$ for the defocusing case. In the subsequent sections we analyze the pattern formation with the latter magic ratio $\sqrt{2}$, i.e., with the additional parameter values

$$\eta=-1, \quad \theta_{cav}=0. \quad (3)$$

With the values given in Eqs. (2) and (3), the linear analysis of Eqs. (1) is reported in Figs. 1(a) where the critical intensity $I_c=|E_s^2|$ is drawn versus the diffraction parameter

$$\theta=\frac{K^2L}{2k}-\theta_{cav}\,. \quad (4)$$

The lowest threshold intensity

$$I_{th}=0.008\,145 \quad (5)$$

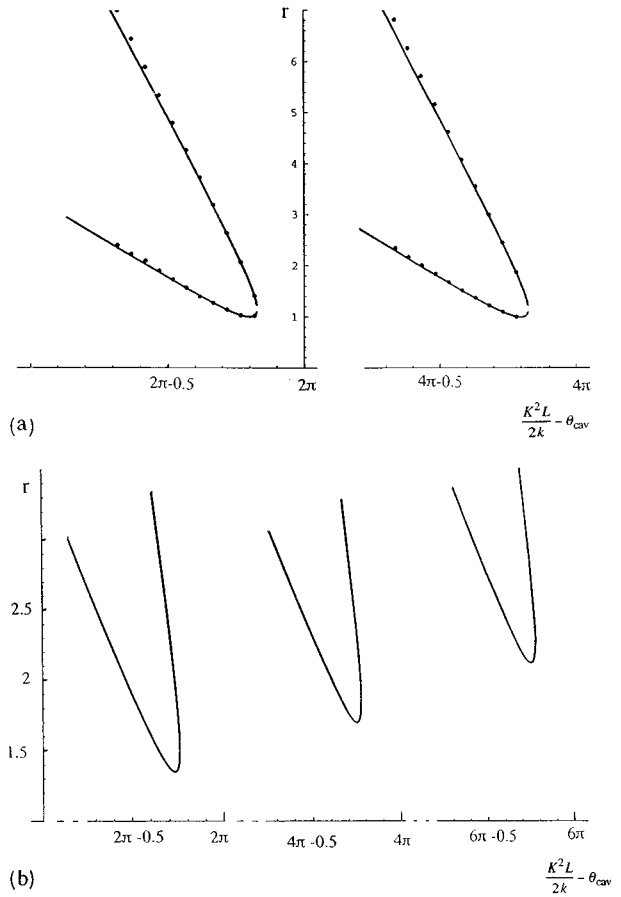

FIG. 1. (a) Marginal stability curve $r=I_c/I_{\text{th}}$ [Eq. (11)], vs $\theta=K^2L/2k-\theta_{cav}$. The linear stability analysis of Eqs. (1) (in dots) and (11) (solid line) are compared. (b) Marginal curve with a Gaussian filter [Eq. (9)] with $a'=5\times10^{-3}$.

corresponds to threshold diffraction parameter values for the successive cones

$$\theta_{th,n}=2n\pi-0.2, \quad (6)$$

with the notations K_{th} and K'_{th} for the first two cones, one has

$$\frac{K'_{th}}{K_{th}}\approx\sqrt{2}. \quad (7)$$

In the following the index ''cr'' refers to any point on the linear boundary, while the index ''th'' is relative to the minimum of the curve. Let us point out that the marginal stability curves in Figs. 1 correspond to a particular case of parameter values [Eq. (2)], and requires numerical investigation. In order to know how the threshold characteristics [Eqs. (5) and (6)] changes with the five parameters of the delay model, a simplified version of Eqs. (1) will now be set up. That version is more tractable for analytical investigations.

In the numerics the emission of the wavelengths on the fourth, fifth... cones are prevented by a filtering procedure. Since our code [11] treats the free-space propagation inside the cavity via a double Fourier transform, a low-pass filter is introduced in the K space at the entrance of the cell, raising the infinite degeneracy predicted at threshold. Two filters are used, either a flat filter with cutoff,

$$F_1(K)=1 \quad \text{for any } K\leqslant K_f, \text{ and 0 elsewhere} \tag{8}$$

or else a diffusion-type filter

$$F_2(K)=\exp[-a'\theta(K)] \tag{9}$$

which removes the degeneracy between the successive minima, as shown in [Fig. 1(b)] for $a'\approx 5\ 10^{-3}$, along the rule $I_{th}\rightarrow I_{th}[1-R'\exp(a'\theta)]$.

B. Comparison with the uniform field model

Near the threshold, the large characteristic time on one hand, and the very small values of I_{th} and $\sin\theta_{th}$ on the other hand, allows [11] to approximate the Ikeda model equations by

$$\partial_{t'}E=E_0'-E+i\beta'\eta|E|^2E+a\left[\exp i\left(\frac{L}{2k}\nabla_T^2-\eta\theta_{cav}\right)-1\right]E \tag{10}$$

or, setting $E=E_s(1+A)$ where E_s is the plane-wave stationary solution of Eq. (10), one obtains

$$\partial_{t'}A=-A+i\eta r(2A+A^*+A^2+2|A|^2+A|A|^2)+ia\sin\left(\frac{L}{2k}\nabla_T^2-\eta\theta_{cav}\right)A, \tag{11}$$

where the time is scaled to the photon lifetime in the ''dressed'' cavity t_{ph} and other parameters are

$$t_{ph}=\frac{d}{1-\rho'},\quad \rho'=\rho e^{-\alpha l/2},\quad E_0'=\frac{E_0}{1-\rho'},$$

$$a=\frac{\rho'}{1-\rho'},\quad \beta'=a\,\frac{\alpha l\Delta}{2},\quad r=\beta'|E_s|^2. \tag{12}$$

Equations (10) and (11) are an extension of the uniform field model introduced by Lugiato and Lefever (LL) [12], for the dispersive ring cavity. In the original (LL) model, the diffraction occurs in the thin nonlinear medium only, then the diffraction term reduces to $ia[(L/2k)\nabla_T^2-\eta\theta_{cav}]$, describing monoconical transverse effects in the focusing case only. Whereas Eq. (10) modelizes diffraction effects occurring mainly in the free space of the cavity, and predicts also transverse instability in the defocusing case.

The operator $\sin[(L/2k)\nabla_T^2-\eta\theta_{cav}]$ is responsible for multicriticality. Indeed at the onset of instability corresponding to $K=K_{th}$ (or $\theta=\theta_{th}$) and $r=r_{th}$, an infinite set of wave numbers K_n such that $\theta(K_n)=\theta_{th}+2\pi n$ become simultaneously unstable. The term $(L/2k)K^2$ may be interpreted in terms of geometrical optics, as the optical path difference between two rays, one propagating along the optical axis of the cavity, the other one being inclined at an angle of K/k with respect to the optical axis. Without any calculation, one can therefore predict that all the rays making an angle equal to K_n/k with respect to the optical axis, may be emitted by the ring cavity device at the onset of instability, since their optical path differ by $2\pi n$.

The marginal stability curve of Eq. (11),

$$r(\Theta)=\frac{-2\Theta\pm\sqrt{\Theta^2-3}}{3} \tag{13}$$

has a minimum for $r_{th}=1$, $\Theta_{th}=-2$.

Let us now compare the instability boundary obtained from Eqs. (1) and (11). They are reported in Fig. 1(a), where the dots are relative to the delay model [with parameters values given by Eq. (2)], the solid line corresponds to Eq. (13) with

$$\Theta=a\,\sin\theta. \tag{14}$$

The value $a=10$, chosen in Fig. 1(a) in order to give a good agreement between the two models, is only 10% higher than the value resulting from relations (2),(3),(12), that is of the order of magnitude of the second-order terms neglected in the derivation of the uniform field model. Thus the threshold characteristics of Eqs. (1) may be generalized for parameter values different from those of Eq. (2), by using the analytical expression in Eq. (13) and the relation (12) between the coefficients of the delay model and those of the uniform field model. In terms of the delay model the minima are thus given by the very simple relation $I_{th}=1/\beta'$, $\theta_{th,n}=\arcsin(-2/a)$.

III. BICONICAL SQUARE PATTERN

The numerical results presented in this paper were obtained with the delay model [Eqs. (1)]. The code uses basically a Crank-Nicholson method for the time integration of Eq. (1b), and a double fast Fourier transform (FFT) calculates the field at time $t+d$ from the data at at time t [Eq. (1a)]. A storage of the data on the whole duration $(t,t-d)$ is necessary in order to derive the solution in the interval $(t,t+d)$. All the results were checked with a spatial grid of 128×128 and 256×256 points, moreover a 384×384 grid was used for the study of the circular input beam. All the patterns described hereafter, are those spontaneously emerging from random noise, moreover, they remain stable in the presence of small noise. The spatial grid size was choosen to be equal to nine times the critical wavelength $\Lambda_{th}=2\pi/K_{th}$, in both directions.

The (4-4) patterns appears with a plane-wave input beam, either with the cutoff filter transparent for the third cone ($K_f\approx\sqrt{3.1}K_{th}$), or with the Gaussian one [Eqs. (8) and (9)]. Both filters may be introduced in the analytical treatment, but for simplicity we have choosen to compare numerical and analytical results only for the case of the cutoff filter.

A. Numerical results

Figures 2 and 3 display the near- and far-field intensity of the (4-4) patterns obtained above threshold for increasing values of the critical parameter

$$\mu=\frac{I-I_{th}}{I_{th}}. \tag{15}$$

The pattern of Fig. 2, called ''straight'' pattern, has the expected critical wavelength $\Lambda_{th}=2\pi/K_{th}$. Figures 2(a) and 2(b) correspond to $\mu=0.1,0.3$ and are stable. Figure 2(c) is obtained for $\mu=0.45$ and is metastable. The Fourier spectra

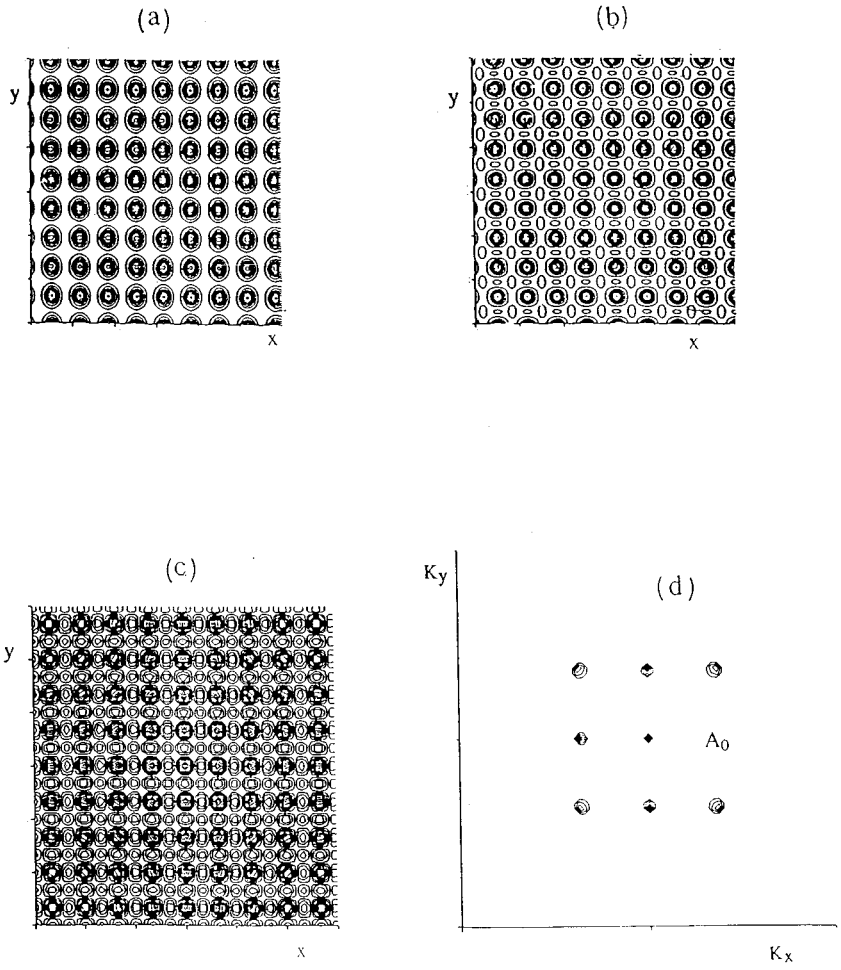

FIG. 2. Numerical biconical (4-4) ''straight'' patterns obtained near the threshold. Near-field intensity contour plots in (a–c), far-field intensity contour plot in (d). The input-field amplitudes are $E_0=0.0125$ (a), 0.015 (b), 0.018 (c). The threshold input for the critical wave number K_{th} of this structure is $E_0^{th}=0.00123$. The peak label A_0 in the far field (d) refers to the discussion in Sec. V.

for the three structures displays two sets of orthogonal modes with wave numbers K_{th} and $\sqrt{2}K_{th}$, oriented along the grid axis and diagonals, respectively [Fig. 2(d)].

After a very long time, the metastable structure in Fig. 2(c) and 2(d) destabilizes, into the pattern in Fig. 3(b) and 3(c) as indicated by the the time trace in Fig. 3(a). The orientation of the intensity peaks in the near- and far-field changes, and slightly smaller wave numbers $\{K_{cr},\sqrt{2}K_{cr}\}$ are observed in the spectrum. We point out that the patterns in Fig. 2 are grid oriented because the grid size is equal to exactly $9\Lambda_{th}$, i.e., fits the preferred wavelength near the threshold. This orientation is choosen while a random noise is added to the plane-wave input profile. At $\mu=0.45$, where the preferred wavelength differs slightly from Λ_{th}, the patterns is not grid oriented [Fig. 3(b) and 3(c)]. The latter ''rotated'' pattern actually exists from $\mu=0.22$ up to $\mu=0.71$, as reported on the numerical amplitude diagram in Fig. 4 (solid lines).

In Figs. 2 and 3 the near-field patterns display a basic square structure, with large modulations of wavelength Λ (Λ_{th} and Λ_{cr}, respectively). The bright peaks are separated by a secondary square structure growing with μ inside this basic structure, with wavelength $\Lambda/\sqrt{2}$. These observations are confirmed by the far-field pattern, which displays, for both patterns, four bright spots on a ring with radius K (K_{th} or K_{cr}), and four less intense spots, in quincunx, on a second ring with radius exactly equal to $\sqrt{2}K$ [Figs. 2(d) and 3(c)].

The Fourier amplitudes of these two numerical patterns are reported in Fig. 4. The amplitudes on the four spots on a given ring are equal. Each amplitude diagram has two branches, the upper one is the amplitude of a spot on the first ring, the lower one, about half the value of the other, is relative to the second ring. The latter property illustrates the biconical character. Therefore an analytical description of the weakly nonlinear regime requires to treat the two sets of modes at the same order, as performed in the next subsections.

B. Amplitude equation for the bisquare

The weakly nonlinear analysis of Eq. (11) in the vicinity of the instability boundary of Fig. 1(a) is detailed for the case of the bisquare pattern. With $\mathbf{A}=(R+iI)e^{\lambda t}$, $\mathbf{V}=(R,I)^t$, the dispersion relation takes the form

$$\mathbf{L}(\lambda,r)\mathbf{V}=\begin{pmatrix} -\lambda-1 & -a\,\sin X-\eta r \\ a\,\sin X+3\,\eta r & -\lambda-1 \end{pmatrix}\begin{pmatrix} R \\ I \end{pmatrix}=0, \quad (16)$$

where $X=(L/2k)\nabla_T^2-\eta\theta_{cav}$. Let $\mathbf{V}^+$ be the eigenvector of the adjoint matrix, with the scalar product $\langle\mathbf{V}_1^+,\mathbf{V}_2\rangle=1/2(\int\mathbf{V}^{+*}{}_1(\vec{x})\mathbf{V}_2(\vec{x})d\vec{x}+\text{c.c.}$ The stationary plane-wave solution E_s becomes unstable to transverse modulations with wave number K, when the intensity r reaches the marginal stability curve in Fig. 1 [Eq. (13)]. Let us be precise that in our problem the choice of the different scalings is not straightforward. The linear growth rate of the perturbation at

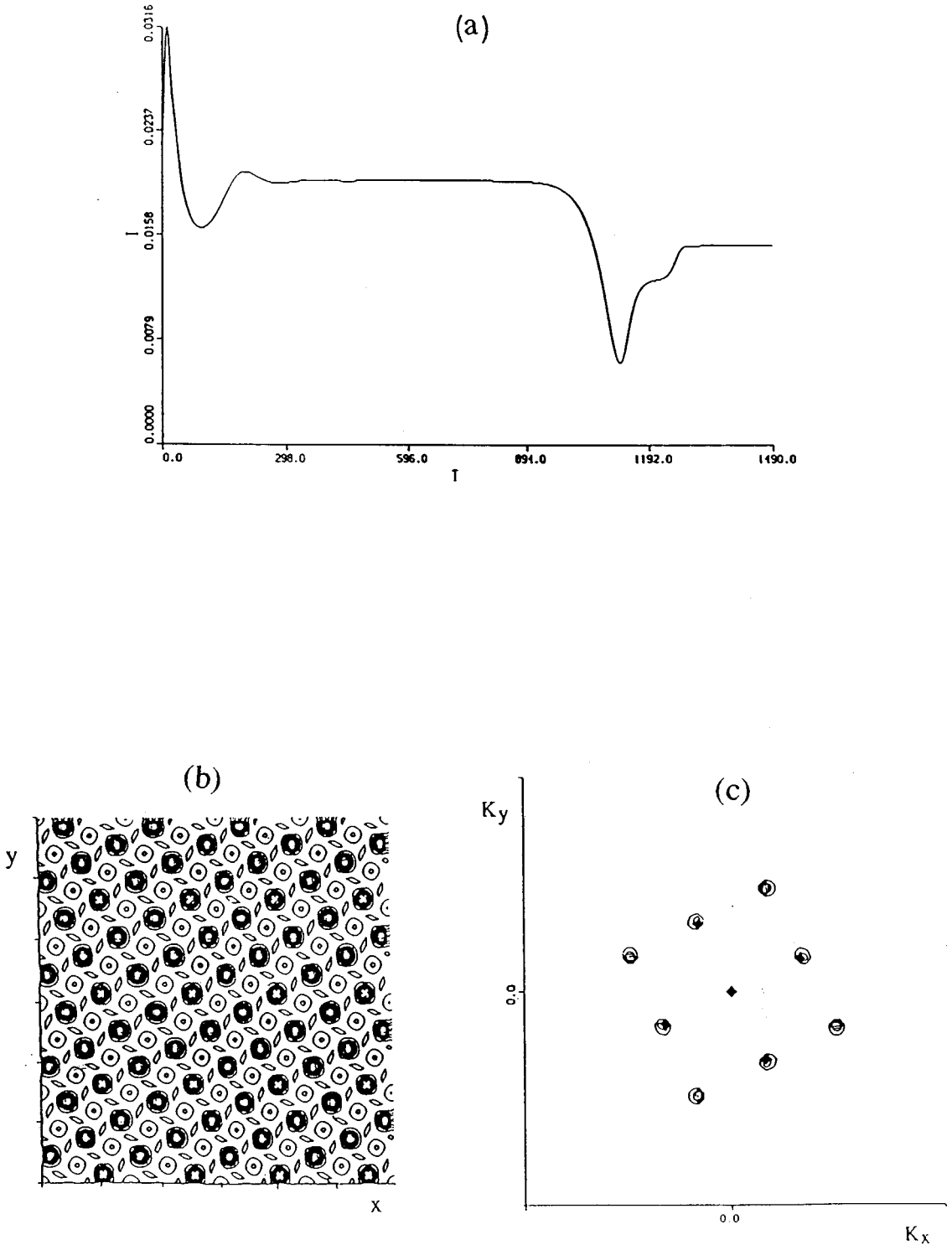

FIG. 3. Numerical biconical (4-4) ''rotated'' patterns, obtained at the first bifurcation from the ''straight'' pattern in Figs. 2, at $E_0=0.018$ for $\Theta=-2.7$. (a) Time trace in $\vec{x}=0$, in units of the round-trip time d of the cavity. (b) Near-field intensity contour plots. (c) Far-field intensity contour plot.

the vicinity of the boundary $r=r_{cr}+\delta r$ $\theta=\theta_{cr}+\delta\theta$, which is supposed to define the scalings [13], is given by the expression

$$\lambda=(2\theta_{cr}-3r_{cr})\delta r+(2r_{cr}-\theta_{cr})\delta\theta. \tag{17}$$

The consistency condition at the lowest order between the time derivative acting on the envelope $\mathbf{A}=\epsilon\mathbf{A}_1+\epsilon^2\mathbf{A}_2$, and the quadratic nonlinearity, should lead to the scaling $T_1=\epsilon t$, $r=r_{cr}+\epsilon r_1+\cdots$. This procedure, reported in Appendix A, gives only qualitative agreement with the numerics as shown in the inserts of Figs. 5. The scaling adopted in the following is the one proposed by Tlidli and Lefever [9], which balances the time derivative with the cubic nonlinearity $T_2=\epsilon^2 t$, and the control parameter with the quadratic nonlinear term $r=r_{cr}+\epsilon r_1+\epsilon^2 r_2$.

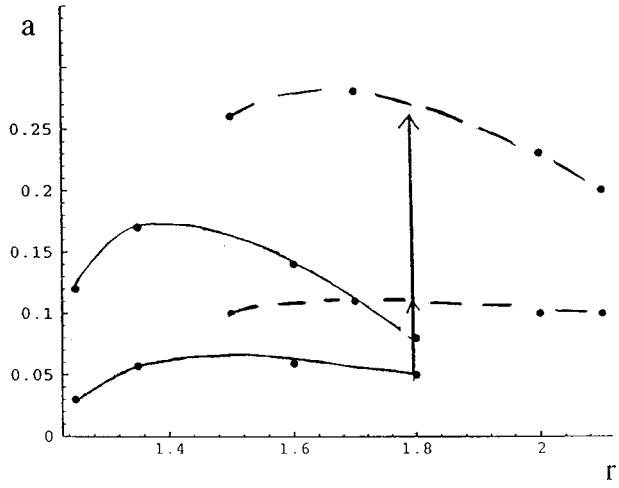

FIG. 4. Numerical amplitudes $\sqrt{I(K_i)/I_s}$ for the modes $(K_{th}, \sqrt{2}K_{th})$ of the ''straight'' pattern (solid line), and for the modes $(K,\sqrt{2}K)$ of the ''rotated'' pattern (dashed lines), vs the critical parameter $r=I/I_{th}$.

At first order, with the notations $\mathbf{A}_1=(R_1+R_1')+i(I_1+I_1')$, or $\mathbf{A}_1=\mathbf{V}_1+\mathbf{V}_1'$, for the complex amplitude, the solution which corresponds to the uniform stationary (4-4) pattern described in the preceding subsection, are of the form

$$R_1=A_1e^{iKx}+B_1e^{iKy}+\text{c.c.}, \tag{18a}$$

$$R_1'=C_1e^{iK(x+y)}+D_1e^{iK(x-y)}+\text{c.c.} \tag{18b}$$

The two sets of active modes with wave numbers K and $K'=\sqrt{2}K$, become linearly unstable at $[r_{cr},\Theta=a\sin\theta(K)]$ and $[r_{cr}',\Theta=a\sin\theta(K')]$, respectively. From now on the calculation only depends on the coupled parameters (Θ,Θ'), which are reported in Fig. 6(a) for the case of the straight pattern, $K=K_{th}$ as the solid and dashed vertical lines. We search the dynamics of the amplitudes $(A=\epsilon A_1,\ B=\epsilon B_1,\ C=\epsilon C_1,\ D=\epsilon D_1)$ for a control parameter value r in the vicinity of r_{cr} and r_{cr}',

$$r=r_{cr}+\epsilon r_1+\epsilon^2 r_2=r_{cr}'+\epsilon r_1'+\epsilon^2 r_2'. \tag{19}$$

The imaginary part of $\mathbf{A}_1$ results from the relations $\{\mathbf{L}(0,r_{cr})\mathbf{V}_1=0;\ \mathbf{L}(0,r_{cr}')\mathbf{V}_1'=0\}$, leading to

$$I_1+I_1'=c(Ae^{iKx}+Be^{iKy})+c'(Ce^{iK(x+y)}+De^{iK(x-y)})+\text{c.c.}, \tag{20}$$

where

$$\left\{c=-\Theta+3\eta r_{cr}=\frac{1}{\Theta-\eta r_{cr}};\quad c'=-\Theta'+3r_{cr}'=\frac{1}{\Theta'-\eta r_{cr}'}\right\}. \tag{21}$$

At second order, Eq. (11) becomes

$$\mathbf{L}(0,r)\mathbf{A}_2=-\mathbf{L}_1(0,r)\mathbf{A}_1-i\eta r\mathbf{N}_2(\mathbf{A}_1)=\begin{pmatrix}f_2\\g_2\end{pmatrix}, \tag{22}$$

with $\mathbf{N}_2(\mathbf{A}_1)=\mathbf{A}_1^2+2|\mathbf{A}_1^2|$, and

$$\begin{pmatrix}f_2\\g_2\end{pmatrix}=\begin{pmatrix}c\\-3\end{pmatrix}\eta r_1R_1+\begin{pmatrix}c\\-3\end{pmatrix}\eta r_1'R_1'-\eta r\times\begin{pmatrix}-2c\mathbf{R}_1^2-2c'\mathbf{R}_1'^2-2(c+c')\mathbf{R}_1\mathbf{R}_1'\\(3+c^2)\mathbf{R}_1^2+(3+c'^2)\mathbf{R}_1'^2+2(3+cc')\mathbf{R}_1\mathbf{R}_1'\end{pmatrix}. \tag{23}$$

Two solvability conditions imply that the vector (f_2,g_2) is orthogonal to the vectors $\mathbf{V}_1^+=(c,1)^t$ and $\mathbf{V}_1'^+=(c',1)^t$. They are of the form $c(f_2)_r+(g_2)_r=c'(f_2)_{r'}+(g_2)_{r'}=0$, where the symbols $(.)_{r,r'}$ stand for the resonant terms on the first and second cone; it gives

$$r_1R_1=r_{cr}\gamma(R_1R_1')_r, \tag{24a}$$

$$r_1'R_1'=r_{cr}'\gamma'(R_1^2)_{r'}, \tag{24b}$$

with

$$\left\{\gamma=-2;\quad \gamma'=-\frac{3+c^2-2cc'}{3-c'^2}\right\}. \tag{25}$$

Particular solutions of Eq. (22) and (23) have Fourier components with wave numbers $\{0,K,\sqrt{2}K,2K,\sqrt{5}K,2\sqrt{2}K\}$. Since the presence of the filter $F_1(K)$ restricts the spectrum to the first two components, we choose the solution $\mathbf{A}_2$ orthogonal to $\mathbf{V}_1$ and $\mathbf{V}_1'$, on the form

$$\mathbf{A}_2=u(1-ic)(R_1R_1')_r+u'(1-ic')(R_1^2)_{r'}+(|A_1^2|+|B_1^2|)\times(g+ip)+(|C_1^2|+|D_1^2|)(g'+ip'), \tag{26}$$

with

$$u=-c'\eta r_{cr};\quad u'=-\frac{1}{2}\eta r_{cr}'(2c+c'\gamma'),$$

$$g=-2r_{cr}\frac{2\eta c+r_{cr}(3+c^2)}{1+3r_{cr}^2} \tag{27}$$

and similar expression for g' with $c\to c'$, $r_{cr}\to r_{cr}'$. The expressions for p,p' are not given because they play no role in the following.

At third order Eq. (11) with $\partial_2=\partial T_2$ gives

$$\mathbf{L}(0,r)\mathbf{A}_3=\partial_2\mathbf{A}_1-\mathbf{L}_1(0,r)\mathbf{A}_2-\mathbf{L}_2(0,r)\mathbf{A}_1-i\eta r_1\mathbf{N}_2(\mathbf{A}_1)-i\eta r\mathbf{N}_3(\mathbf{A}_1,\mathbf{A}_2), \tag{28}$$

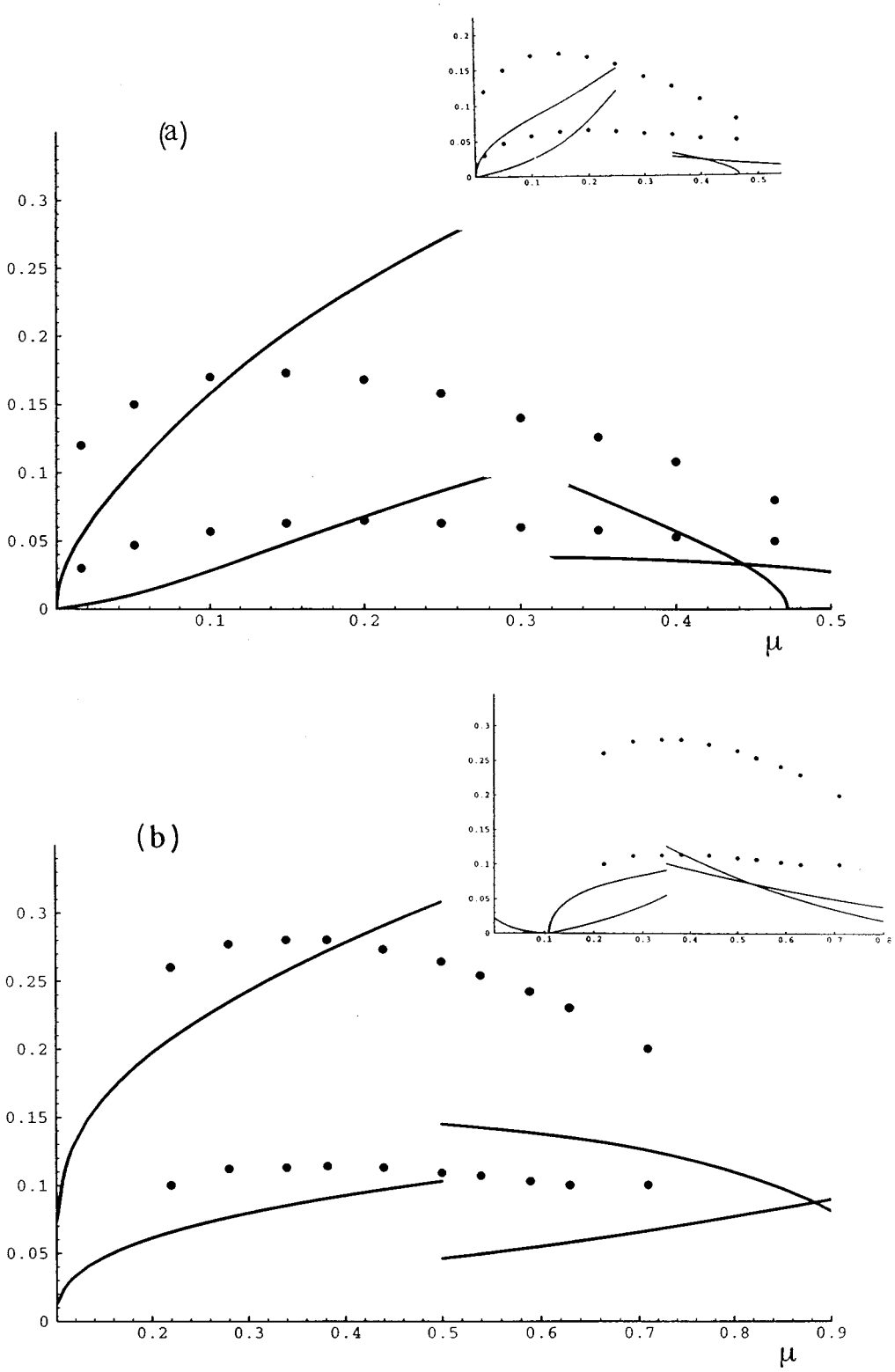

FIG. 5. Nonlinear analysis of the bisquare structure. Comparison between the analytical and numerical results. The moduli of the two Fourier components $|\mathbf{A}|$ and $|\mathbf{C}|$ for the coupled set of modes with wave numbers $(K,\sqrt{2}K)$, Eqs. (36)–(40), are reported in solid lines, vs the control parameter $\mu=I/I_c-1$; the numerical results taken from Fig. 4, are reported in dots. (a) ''Straight'' pattern amplitude diagram for $\Theta=-2$, $\Theta'=-4$, (modes K_{th}, $\sqrt{2}K_{th}$). The coefficients in Eqs. (21),(25),(36) are, in the left part, $r_{cr}=1$, $r'_{cr}=1.45$; $c=-1$, $c'=-0.4$; $\gamma=-2$, $\gamma'=-1.15$; $\lambda=0.6$, $\lambda'=-0.1$; $\delta=-20$, $\delta'=-5.5$; $\sigma=-8.5$, $\sigma'=-7$; in the right part, $r_{cr}=1.66$, $c=-3$, $\Theta=-2$, $r'_{cr}=1.45$, $c'=-0.4$, $\Theta'=-4$, $\gamma=-2$, $\gamma'=-3.35$; $\lambda=0.6$, $\lambda'=-0.1$; $\delta=5.5$, $\delta'=-5$; $\sigma=10$, $\sigma'=-10$. (b) ''Rotated'' pattern amplitude diagram for $\Theta=-2.7$, $\Theta'=-5.4$. In the left part, $\gamma'=-1$; $\lambda=0.8$, $\lambda'=0.1$; $\delta=-14$, $\delta'=-5$; $\sigma=-5$, $\sigma'=-5$; in the right part, $\gamma'=-15$; $\lambda=1.5$, $\lambda'=0.1$; $\delta=105$, $\delta'=-5$; $\sigma=6$, $\sigma'=-5$. The insets compare the numerics with the analytical diagrams derived in Appendix A. The axes refer to the same variables as in the main figures.

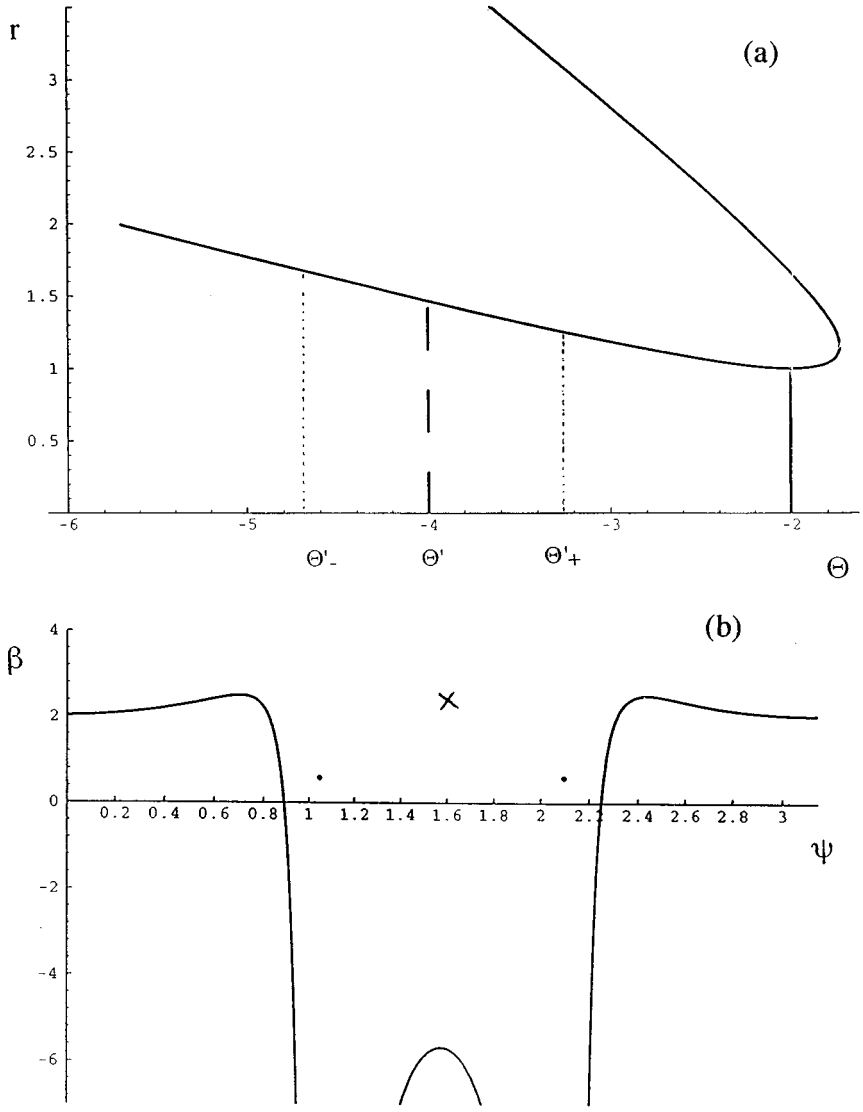

FIG. 6. (a) Linear instability boundary. Scheme of the modal interaction in the diagram $r(\Theta)$. The mode with critical wave number K_{th} corresponds to the solid line $\Theta_{th}=-2$. For $\Psi=\pi/2$, the mode $\sqrt{2}K_{th}$, corresponds to the dashed line $\Theta_{th}=-4$. For $\Psi\neq\pi/2$, the two modes $K'_{\pm}$ correspond to the dotted lines. (b) Angular coupling function $\beta(\Psi)$ [defined in Eq. (42)]. The solid line and the dots are relative to a monoconical pattern, the cross to a biconical (4-4) structure.

with $\mathbf{N}_3(\mathbf{A}_1,\mathbf{A}_2)=2(\mathbf{A}_1\mathbf{A}_2+\mathbf{A}_1\mathbf{A}_2^*+\mathbf{A}_1^*\mathbf{A}_2)+\mathbf{A}_1|\mathbf{A}_1^2|$, leading to the solvability conditions

$$\frac{2c}{3-c^2}\,\partial_2 R_1=\eta\left[r_2R_1+\frac{3+c^2}{3-c^2}\,r_1R_2+2(R_1R_1')_r r_1+r_{cr}W\right], \tag{29a}$$

$$\frac{2c'}{3-c'^2}\,\partial_2 R_1'=\eta\left[r_2'R_1+\frac{3+c'^2}{3-c'^2}\,r_1'R_2'-\gamma(R_1^2)r\,\frac{3+c^2-2cc'}{3-c'^2}\,r_1+r_{cr}'W'\right], \tag{29b}$$

$$W=\frac{e}{u'}\,(R_1R_2')_r+\frac{f}{u}\,(R_2R_1')_r+h(R_1R_1'^2)_r+j(R_1^3)_r+GR_1, \tag{30a}$$

$$W'=\frac{e'}{u}\,(R_1R_2)_{r'}+h'(R_1'R_1^2)_{r'}+j'(R_1'^3)_r+GR_1', \tag{30b}$$

$$G=2[g(|A_1^2|+|B_1^2|)+g'(|C_1^2|+|D_1^2|)] \tag{30c}$$

and

$$e=2u',\quad e'=2\frac{3-c^2}{3-c'^2}\,u\quad j=\frac{1-c^4}{3-c^2};\quad j'=\frac{1-c'^4}{3-c'^2}; \tag{31a}$$

where

$$f=2u\,\frac{3+c^2-2cc'}{3-c^2},\quad h=1+c'^2\,\frac{1-3c^2}{3-c^2},$$

$$h'=1+c^2\,\frac{1-3c^2}{3-c'^2}. \tag{31b}$$

The addition of the solvability conditions at the second and third order [Eqs. (24) and (29)], multiplied by ϵ^2 and ϵ^3, respectively, leads to the following set of coupled equations for the amplitudes of the Fourier modes:

$$\begin{aligned}\partial_\tau A=&\mu A+\gamma_A\tfrac{1}{2}(B^*C+BD)+2(h+f\,)A^*DC\\&+A[(2g+3j)|A^2|+(4e+2g+6j)|B^2|\\&+(2g'+2h+f\,)(|C^2|+|D^2|)],\end{aligned} \tag{32a}$$

$$\begin{aligned}\partial_\tau B=&\mu B+\gamma_A\tfrac{1}{2}(A^*C+AD^*)+2(h+f\,)B^*CD^*\\&+B[(2g+3j)|B|^2+(4e+2g+6j)|A^2|\\&+(2g'+2h+f\,)(|C^2|+|D^2|)],\end{aligned} \tag{32b}$$

$$\begin{aligned}\zeta\partial_{\tau'}C=&\mu' C+\gamma_C AB+(DB^2+D^*A^2)(e'+h')\\&+C[(2g'+2h'+e')(|A^2|+|B^2|)+(3j'+2g')\\&\times|C^2|+(6j'+2g')|D^2|],\end{aligned} \tag{32c}$$

$$\begin{aligned}\zeta\partial_{\tau'}D=&\mu' D++\gamma_C AB^*+(CB^{*2}+C^*A^2)(e'+h')\\&+D[(2g'+2h'+e')(|A^2|+|B^2|)\\&+(6j'+2g')|C^2|+|(3j'+2g')D^2|],\end{aligned} \tag{32d}$$

where the time is scaled as $\tau=t[r_{cr}\eta(3-c^2)/2c]$, $\zeta=[r_{cr}c'(3-c^2)/r'_{cr}c(3-c'^2)]$ and the coefficients $\gamma_{A,C}$ depend on the control parameter value,

$$\{\gamma_A=-2\gamma(1+\lambda\mu),\quad \gamma_C=-2\gamma'(1+\lambda'\mu)\}, \tag{33a}$$

$$\left\{\lambda=1-\frac{(3+c^2)u}{\gamma(3-c^2)}\quad \lambda'=1-\frac{(3+c'^2)u'}{\gamma'(3-c'^2)}\right\}. \tag{33b}$$

Numerical patterns have $\vec{x}\to-\vec{x}$ symmetry in the near field, and $K\to-K$ in the far field and satisfy $|A|=|B|$, $|C|=|D|$. Therefore among the solutions of Eqs. (32) we choose solutions with real A,B,C,D leading either to solutions like

$$\{A,A,C,C\}\ \text{named solution ``+''}, \tag{34}$$

or to

$$(A,-A,C,C\},\ \text{or}\ \{A,A,-C,-C\}\ \text{named solution ``−''} \tag{35}$$

The first set, [Eq. (34)], gives two real coupled equations

$$\partial_\tau A=\mu A+\gamma_A AC+A(\delta A^2+\sigma C^2), \tag{36a}$$

$$\zeta\partial_\tau C=\mu' C+\gamma_C A^2+C(\delta' C^2+\sigma' A^2), \tag{36b}$$

where

$$\{\delta=4e+4g+9j,\delta'=2g'+9j\},$$

$$\{\sigma=4f+4g'+6h,\sigma'=4e'+4g'+6h'\}, \tag{37}$$

and the second set [Eq. (35)], leads to a system identical to Eqs. (36) except $(\gamma_A,\gamma_C)\to(-\gamma_A,-\gamma_C)$, whose solutions are the opposite of Eqs. (36), so that all the symmetrical solutions of Eqs. (32) can be deduced from the single set of Eqs. (36). The ''+'' solutions of Eqs. (32) are the solutions (A,C) of Eqs. (36), whereas the ''−'' solutions of Eqs. (32) are $(-A,-C)$.

In Eqs. (36) the quadratic coupling terms describe the resonant interaction between the modes of K and $\sqrt{2}K$, and negative values of δ, σ, δ', σ' ensure the stability for positive values of μ. The bifurcation diagram of Eqs. (36) have been studied [14–16] in the context of one-dimensional transverse codimension two modal interactions. Moreover, basic mechanisms that generate a secondary drift instability were reported by Fauve, Douady, and Thual [17].

Let us now compare the stationary solutions of Eqs. (36) with the numerical diagrams of Fig. 4 which display a (4-4) pattern for a very large range of the critical parameter r $(1\leqslant r\leqslant 1.7)$. Let us first notice the unusual shape of the instability boundary $r(\Theta)$ drawn in Fig. 6(a), which displays two branches r^+_{cr} and r^-_{cr} located one above the other. The growth of any mode with wave number K obviously depends on the two critical parameters $(r-r^+_{cr})$ and $(r-r^-_{cr})$. Consequently a correct treatment of the coupled amplitude equations should involve tricriticality, whereas Eqs. (36) are derived in a bicritical frame.

Secondly the relevant variable for the analytical treatment is not K, or K^2, as usual, but $\Theta=10\sin\theta(K)$. It follows that while the ratio of the critical wave numbers for the two cones differs from $\sqrt{2}$ by less than 1%, the two sets of modes $\{K,\sqrt{2}K\}$ are not at exact resonance, on the contrary, their critical parameters r_{cr}(K) and $r'_{cr}(\sqrt{2}K)$ noticeably differ. In terms of the analytical variables the relevant threshold values for the ''straight'' pattern correspond to,

$$\Theta=-2,\quad \Theta'=-4 \tag{38}$$

cf. the scheme in Fig. 6(a), and for the ''rotated'' pattern to

$$\Theta=-2.7,\quad \Theta'=-5.4, \tag{39}$$

The analytical amplitudes for the K, $\sqrt{2}K$ modes

$$|\mathbf{A}(\mu)|=|(1+ic)A+(1-ic)uAC)|, \tag{40a}$$

$$|\mathbf{C}(\mu)|=|(1+ic')C+(1-ic')u'A^2)| \tag{40b}$$

are drawn in Figs. 5(a) and 5(b) for the straight and rotated patterns, respectively. The two parts of the diagrams are calculated by refering to the closest boundary, i.e., the left part of each diagram is calculated for $r(\Theta)$ close to the lower boundary $(r_{cr}=r^-_{cr})$, whereas the right corresponds to $r(\Theta)$ close to the upper branch $(r_{cr}=r^+_{cr}$, $r'_{cr}=r^-_{cr})$. The two analytical branches fit the numerical results near each boundary, and finally reproduce fairly well the numerical results (in dots). In fact, in the middle of the diagram $(r^-_{cr}<r<r^+_{cr})$, the dots are located in between the left and right curves, that is, the signature of tricriticality. Nevertheless, the numerical

results are globally reproduced by our bicritical analysis, in the sense that the analytical amplitudes are of the same order of magnitude, $|\mathbf{C}(\mu)|\approx(1/2)|\mathbf{A}(\mu)|$ in the whole domain of existence of the patterns, and the treatment reproduces the unusual bell-shape diagram.

The inserts in Figs. 5 are the diagrams obtained with the scaling $\partial_t \approx r - r_{cr} \sim \epsilon$. The derivation is given in Appendix A. The results display clearly the relevance of the scaling ($\partial_t \approx \epsilon^2, r - r_{cr} \approx \epsilon$) treated in this section.

C. Angular coupling

Square patterns were already observed in the monoconical emission of the ring cavity on the focusing side [8,9], but they were unstable, and destabilized help to a slight noise, into a hexagonal pattern. The stabilization of squares due to the $(K,\sqrt{2}K)$ intermode coupling is now illustrated by comparing the mono- and biconical coupling coefficient $\beta(\psi)$ between two wave vectors $\vec{K}_i$ and $\vec{K}_j$ belonging to the first cone, with vertex angle ψ. Let us define first the angular coupling function. With the notation $A = R + iI$ and

$$R = A_i e^{i\vec{K}_i\vec{x}} + A_j e^{i\vec{K}_j\vec{x}} + \text{other terms} + \text{c.c.} \tag{41}$$

the coupling function appears in the amplitude equations

$$\partial_\tau A_i = \mu A_i + \delta A_i(|A_i^2| + \beta(\psi)|A_j^2|) + \text{other terms}. \tag{42}$$

Let us first deduce from Eq. (32a) the value of the biconical coupling coefficient between the two orthogonal modes $\beta^{bic}(\pi/2)$,

$$\beta^{bic} = (4e + 2g + 6j)/(2g + 3j) \tag{43}$$

which is about 2.5 for any $K \approx K_{th}$ [cross in Fig. 6(b)]. The general derivation of $\beta^{bic}(\psi)$ for a vertex angle close but different from $\pi/2$ is given in Appendix B. The curves for different values of K near K_{th}, are very narrow around $\psi \approx \pi/2$ because the biconical coupling function $\beta^{bic}(\psi)$ does not exist outside a very tiny domain around $\psi = \pi/2$, as deduced from Figs. 1 and relations (6). More precisely for $K = K_{th}$ the biconical emission concerning the first two cones is only possible for

$$\psi = 90° \pm 1°. \tag{44}$$

The monoconical coupling function $\beta(\psi)$, derived in Appendix C, is drawn in Fig. 6(b). One may observe the three following points:

(a) The value $\beta(\pi/3)$, indicated in dots, smaller than unity, ensures the coexistence of the two adjacent wave vectors. This result agrees with the observation of monoconical hexagons.

(b) $\beta(53°) \approx 0$. This result will be used in our interpretation of the (8-8,12) pattern formation.

(c) The large negative value of $\beta(\pi/2)$ forbids the formation of monoconical squares. The monoconical analysis is thus unable to reproduce the numerical observations of biconical structures.

Let us notice that (LL) model Eq. (11) and also the amplitude equations (32) do not display the variational structure. Therefore the coupling function $\beta(\psi)$ cannot be invoked to predict the more stable pattern, as it was done in the feedback-mirror device [5], for example. Nevertheless, the present study shows that the coupling coefficient between two orthogonal wave vectors increases from -6 up to $+2.5$ when the pattern formation changes from a mono- into a biconical one. Therefore the role of the $(K,\sqrt{2}K)$ coupling is to stabilize the square pattern.

Let us now discuss the possible $K - \sqrt{3}K$ coupling that was not investigated in the above study, but must be considered since the cutoff filter is transparent for the third cone having a wave number ratio K''_{th}/K_{th} equal to 3.1. One could expect that the $(K,\sqrt{3}K)$ coupling either enforces the hexagonal structure, or that a tricritical bifurcation involving an intermodal $(K,\sqrt{2},K\sqrt{3}K)$ interaction, leads to a twelvefold orientational order quasipattern. Actually none of these structures was observed in our simulations, while a biconical ''3.1'' structure (with wave number ratio $\sqrt{3.1}$) was obtained, which has a rhombus on the second cone (with vertex angle 57°), and a roll on the third cone, located in the bisector of this vertex angle. This stable ''3.1'' structure was observed by a two-step procedure: the profile defining the initial conditions of the intracavity field is first obtained by integration of Eqs. (1) (with plane-wave input plus a small random noise) without any filter. In the transient, all the unstable wavelengths grow simultaneously, leading to a multiconical ''noisy'' intracavity profile. Then the numerical simulation starts again with this multiconical noise as initial conditions, and with the cutoff filter (transparent for the first, second, and third cone). The study of such structure is out of our purpose, but one can conjecture that the strong resonant coupling of the 3.1 structure, with two critical modes having the same threshold, $r''/r = 1$ explains why it wins versus the hexagonal order. A $(K,\sqrt{3}K)$ structure with threshold ratio $r''/r = 2$ [see Fig 6(a), $(\Theta = -2, \Theta'' = -6)$], would correspond to a much weaker biconical coupling process.

D. Drift bifurcation

Why does the ''first'' pattern with wave numbers $\{K_{th},\sqrt{2}K_{th}\}$ rotate at $r = 1.43$? The above nonlinear analysis displays real amplitude A for $r \leqslant 1.48$ [Fig. 5(a)], that could explain this observation. Actually we demonstrate that the rotation of the ''straight'' pattern actually occurs before $r = 1.48$, due to the onset of a drift bifurcation, when the real solutions get unlocked phases. In the context of one dimensional $(K,2K)$ modal competition, drifting solutions with complex amplitudes (unlocked phases) were predicted to emerge from real amplitudes [14–16] solutions. They were shown to grow because the $2K$ modes are not sufficiently damped, but they are generally unstable and thus difficult to observe [17].

A very simple qualitative approach to predict the onset of the drift instability, or the growth of the $\sqrt{2}K$ modes, consists in the observation of the linear threshold boundary. The boundaries, for both $\{K,\sqrt{2}K\}$ modes, or $r(\Theta)$ and $r(2\Theta)$ curves, are drawn in Fig. 7(a). The domain inside the solid line corresponds approximately to the stable domain for the two modes. An analytical study of the drift onset actually requires more investigation than the linear analysis itself, since drift bifurcation occurs when the solutions of Eqs. (32) loose the reflexion symmetry, or the A,B,C,D amplitudes loose their phase-locked property. In order to investigate the bifurcation towards complex solutions, we write

$A=R_a e^{i\phi_a}$, $B=R_b e^{i\phi_b}$, $C=R_c e^{i\phi_c}$, $D=R_d e^{i\phi_d}$, $\Sigma=\phi_c-(\phi_a+\phi_b)$, $\Delta=\phi_d-(\phi_a-\phi_b)$, in Eqs. (32) or

$$\partial_\tau R_a+iR_a\partial_\tau\phi_a=\mu R_a+\tfrac{1}{2}\gamma_A R_b(R_d e^{i\Delta}+R_c e^{i\Sigma}) +2R_aR_cR_d(h+f\,)e^{i(\Sigma+\Delta)}+Af_a, \quad (45a)$$

$$\partial_\tau R_b+iR_b\partial_\tau\phi_b=\mu R_b+\tfrac{1}{2}\gamma_A R_a(R_d e^{-i\Delta}+R_c e^{i\Sigma}) +2R_bR_cR_d(h+f\,)e^{i(\Sigma-\Delta)}+Bf_b, \quad (45b)$$

$$\zeta\partial_\tau R_c+iR_c\partial_\tau\phi_c=\mu' R_c+\gamma_C R_aR_b e^{-i\Sigma}+R_d[R_b^2e^{-i(\Sigma-\Delta)} +R_a^2e^{-i(\Sigma+\Delta)}](e'+h')+Cf_c, \quad (45c)$$

$$\zeta\partial_\tau R_d+iR_d\partial_\tau\phi_d=\mu' R_d+\gamma_C R_aR_b e^{-i\Delta}+R_c[R_b^2e^{i(\Sigma-\Delta)} +R_a^2e^{-i(\Sigma+\Delta)}](e'+h')+Df_d, \quad (45d)$$

where f_i are real functions of R_i independent of Σ and Δ. The phases obey

$$\partial_\tau\Sigma=-\gamma_C\frac{R_aR_b}{\zeta R_c}\sin\Sigma-\gamma_A R_c\left(\frac{R_b}{2R_a}+\frac{R_a}{2R_b}\right)\sin\Sigma -\gamma_A\frac{R_d}{2}\left(\frac{R_b}{R_a}-\frac{R_a}{R_b}\right)\sin\Delta+(e'+h')\frac{R_d}{\zeta R_c}[R_b^2\sin(\Delta-\Sigma)-R_a^2\sin(\Delta+\Sigma)]-2(h+f\,)R_dR_c[\sin(\Delta+\Sigma)+\sin(\Sigma-\Delta)] \quad (46a)$$

and

$$\partial_\tau\Delta=-\gamma_C\frac{R_aR_b}{\zeta R_c}\sin\Delta-\gamma_A R_d\left(\frac{R_b}{2R_a}+\frac{R_a}{2R_b}\right) \times\sin\Sigma-\gamma_A\frac{R_c}{2}\left(\frac{R_b}{R_a}-\frac{R_a}{R_b}\right)\sin\Sigma -(e'+h')\frac{R_d}{\zeta R_c}[R_b^2\sin(\Delta-\Sigma)-R_a^2\sin(\Delta+\Sigma)] -2(h+f\,)R_dR_c[\sin(\Delta+\Sigma)-\sin(\Sigma-\Delta)] \quad (46b)$$

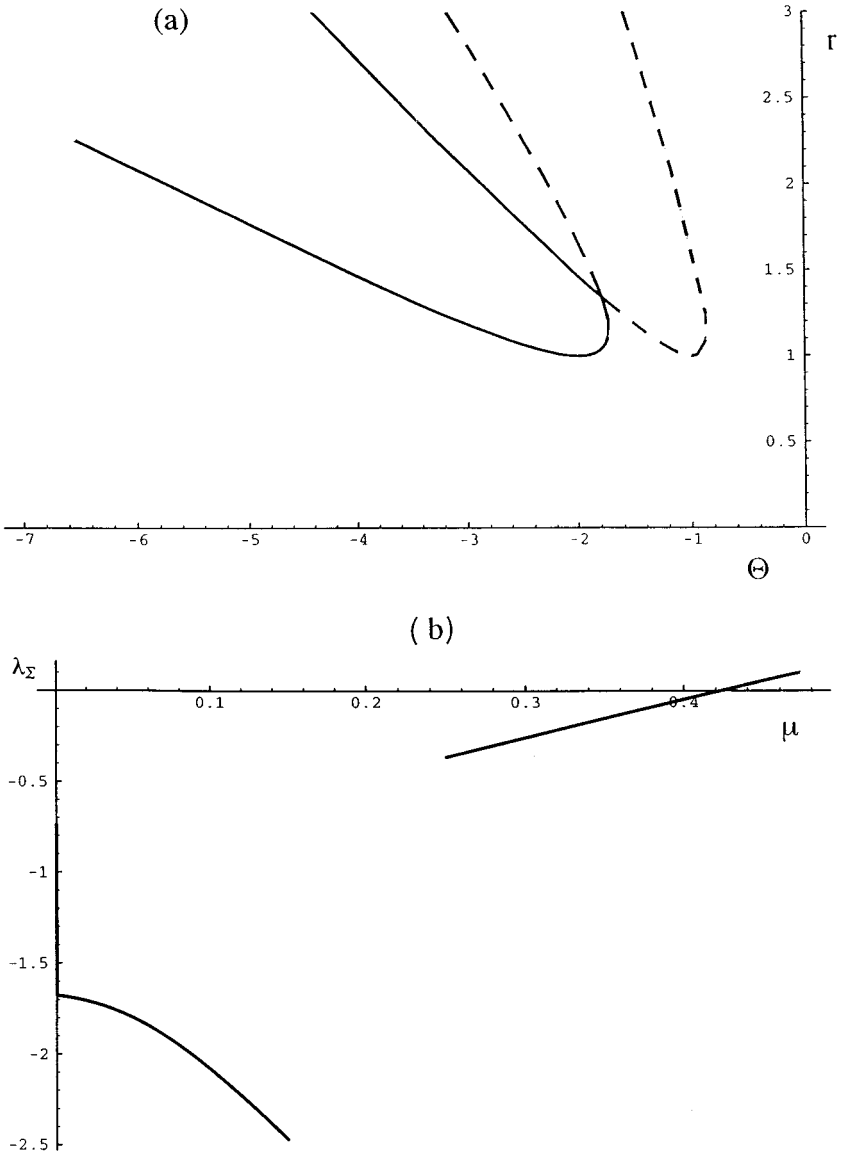

FIG. 7. Drift bifurcation threshold. (a) Linear boundaries of the K and $\sqrt{2}K$ instability, or $r(\Theta)$ and $r(2\Theta)$ functions [Eq. (13)]. (b)-(c) Linear growth rate λ_Σ of the phases Σ, Δ [Eq. (47)] versus $u=I/I_{cr}-1$ for the ''straight'' and ''rotated'' bisquare patterns, respectively.

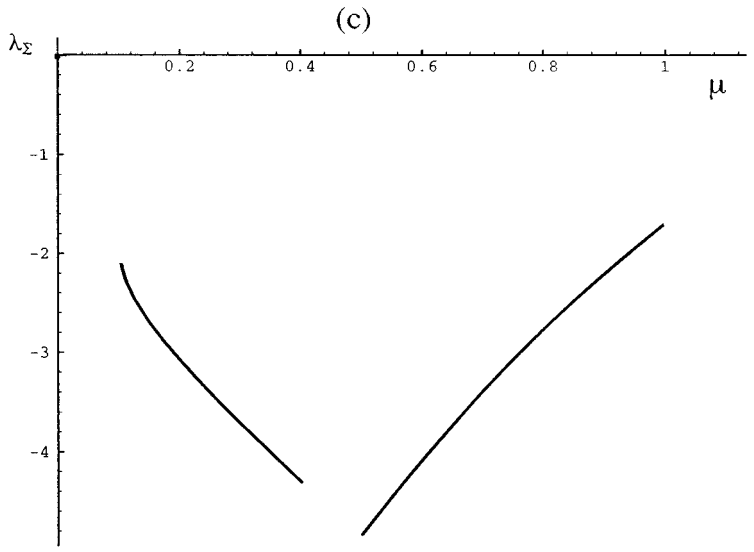

FIG. 7 (*Continued*).

and two equations for (ϕ_a, ϕ_b).

In our problem, near the lower branch, when μ becomes positive, the null state is expected to bifurcate towards a stable ''+'' or ''−'' solution described by Eqs. (36) which corresponds to the ''mixed modes'' introduced by Armbruster, Guckenheimer, and Holmes [15]. They have reflexion symmetry, since by the appropriate change of coordinate Eq. (11) takes the form $R = R_a \cos Kx + R_b \cos Ky + R_c \cos[K(x+y)+\Sigma] + R_d \cos[K(x-y)+\Delta]$. The stability of the mixed modes will now be investigated.

The linearization of Equations (45) and (46) gives

$$\partial_\tau \Sigma = \lambda_\Sigma \Sigma, \quad \partial_\tau \Delta = \lambda_\Sigma \Delta,$$

with a linear growth rate

$$\lambda_\Sigma = -\frac{1}{\zeta}\left(2e' + 2h' + \frac{\gamma_C}{R_c}\right) R_a^2 - \gamma_A R_c - 4(h+f)R_c^2. \tag{47}$$

If λ_Σ is negative the real solutions are stable, but when λ_Σ becomes positive a new state emerges, characterized by

$$\partial_\tau R_{a,b,c,d} = 0, \quad \partial_\tau \Sigma = \partial_\tau \Delta = 0,$$

$$\text{but } \partial_\tau \phi_a \text{ and } \partial_\tau \phi_b = \text{const}, \tag{48}$$

which has no reflexion symmetry, and the pattern may drift with constant velocities $d_\tau \phi_a$ and $d_\tau \phi_b$ in the x and y directions, respectively, with

$$\partial_\tau \phi_a = (\gamma_A/2 + (h+f)R_c)R_c(\Sigma + \Delta), \tag{49a}$$

$$\partial_\tau \phi_b = (\gamma_A/2 + (h+f)R_c)R_c(\Sigma - \Delta). \tag{49b}$$

The evolution of the growth rate λ_Σ calculated with the analytical values of (A,C) of Figs. 5(a) and 5(b), is reported in Figs. 7(b) and 7(c), for the straight and rotated patterns, respectively. In the left part of the diagrams, only the ''+'' solution is stable, with negative values of $\lambda_\Sigma < 0$ reported on the left of Figs. 7(b) and 7(c). In the right part of the diagrams, only the ''−'' solution is stable, and for the case of Fig. 7(b), λ_Σ becomes positive at $r = 1.43$, where the straight pattern rotates. In agreement with the qualitative prediction, the drift bifurcation occurs close to the upper solid boundary of Fig. 7(a). Finally the growth rate study allows to select between the ''+'' and ''−'' solutions, near each boundary, moreover, it predicts that the real solution for the straight pattern becomes unstable for A and $C \neq 0$, as numerically observed.

No drifting solution was observed numerically. This can be explained by the Fauve, Douady, and Thual analysis [17] who have shown that ''even if the bifurcation is supercritical, the homogeneous drifting solution is generally unstable, and the propagation of drifting inclusions changes the wave number, thus stabilizating a new static pattern''. Actually we have not investigated the transient solutions near $t \approx 1200\ d$, but a new static pattern stabilizes at $r \approx 1.43$ with a wave number located inside the solid lines of Fig. 7(a).

In the case of the ''rotated'' pattern the growth rate of the ''+'' solution in the left part, and of the ''−'' solution in the right part, are negative for the whole domain of the existence of the bisquare [Fig. 7(c)]. The bifurcation of this pattern will be described in the next section.

IV. BICONICAL (8-8) AND (8-12) PATTERNS

The (4-4) rotated structure with $\Theta(K) = -2.7$ is observed in a large domain, from the linear threshold $r_{cr} \approx 1.2$ until $r \approx 1.7$, with both filters $F_{1,2}(K)$. At $E_0 = 0.022$ it destabilizes into two stationary periodic (8-8) and (8-12) patterns, depending on the filter functions used in the code.

A. (8-8) pattern

Let us first describe the (8-8) pattern obtained with the gaussian filter, [Eq. (9)]. At $E_0 = 0.022$ the near field has reflection symmetry, [Fig. 8(a)–8(c)] but it looses this property at $E_0 = 0.024$ [Fig. 8(d)], and destabilizes into rolls at $E_0 = 0.025$. Surprisingly the spatial period in Fig. 7 is neither equal to $\Lambda = 2\pi/K$ corresponding to the first cone, nor the $\Lambda/\sqrt{2}$ corresponding to the second cone, but to 2.23 Λ, and the large intensity peaks are not aligned along the wave vec-

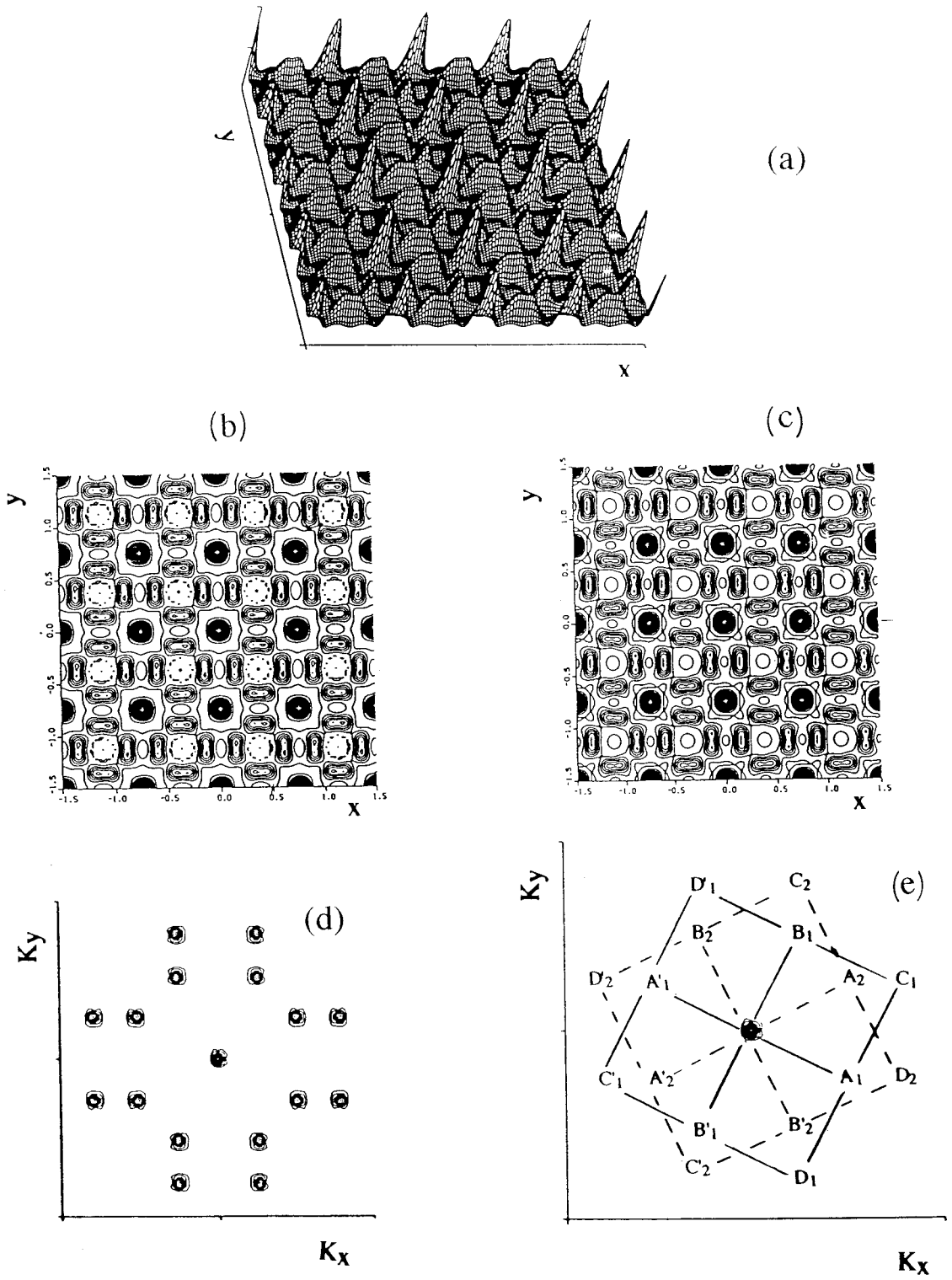

FIG. 8. Mode-locked (8-8) periodic structure obtained with the Gaussian filter [Eq. (9), with $a'=5\times10^{-3}$], in the range $0.023 \leqslant E_0 \leqslant 0.024$. (a) and (b) Near-field intensity, in 3D graph and contour plots for $E_0=0.023$. (c) Near-field intensity for $E_0=0.024$. The pattern is still periodic, but a slight curvature in the contour plots indicates the onset of the phase instability, or the loss of the $\vec{x} > -\vec{x}$ symmetry. A very slow evolution of the time trace, scarcely visible after integration over several thousands of photon lifetime, might be the signature of a drifting solution. (d) and (e) Far-field contour plots.

tors but along the grid axis. The explanation lies in the observation of the spectrum, which consists in two bisquare patterns twisted by an angle equal to 53° (mod. $\pi/2$), with equal amplitudes on each ring. With the notations of Fig. 8(e), the wave vectors responsible for the large period 2.23 Λ are the orthogonal vector sets $(\overrightarrow{C_1A_2},\overrightarrow{D_2A_1})$, and $(\overrightarrow{D_1B_2'},\overrightarrow{C_2'B_1'})$ and the symmetrical ones. They are actually locked to other vectors by the relation

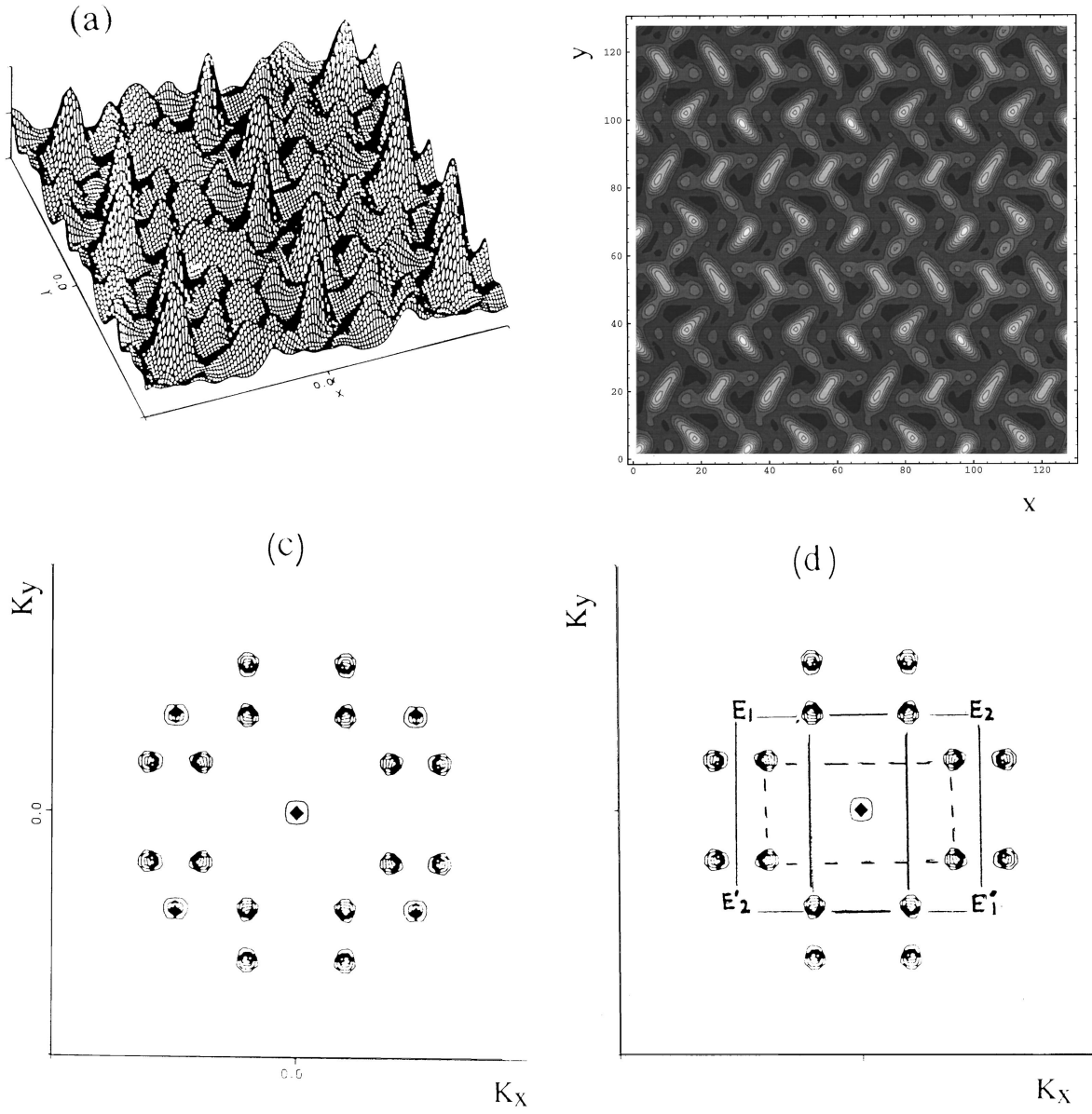

FIG. 9. Mode-locked periodic (8-12) structure obtained with the flat filter F_1 [Eq. (8)]. Near-field 3D view in (a), and contour plot in (b), far-field intensity contour plot in (c) and (d) for $E_0=0.022$. The time trace is constant for $E_0=0.022$, but a very slow evolution is observed for $E_0=0.023$.

$$\vec{K}_{\text{lock1}}=\overrightarrow{D_1B_2'}=\tfrac{1}{2}\overrightarrow{A_1A_2}=\tfrac{1}{4}\overrightarrow{B_2'B_1}=\tfrac{1}{8}\overrightarrow{D_1C_2}, \qquad (50a)$$

$$\vec{K}_{\text{lock2}}=\overrightarrow{C_1A_2}=\tfrac{1}{2}\overrightarrow{B_1B_2}=\tfrac{1}{4}\overrightarrow{A_2A_1'}=\tfrac{1}{8}\overrightarrow{C_1D_2'} \qquad (50b)$$

and similar equations for $\overrightarrow{D_2A_1}$, and $\overrightarrow{C_2'B_1'}$. The far field in Fig. 8(d) may be seen as the superposition of the two ''rotated'' (4-4) patterns, with angles $\pm$arctg1/2, emerging from the ''straight'' one. The stability of the total structure being warranted by the vectorial mode-locking relation in Eqs. (50).

A question arises: why does the eight spots are not regularly distributed on each circle, as in the case reported by Müller and recently observed [5–6]? The main reason probably lies into the mode-locking process which favors the 53° (mod. $\pi/2$) orientational order. Let us also consider the role of the coupling coefficient $\beta(\psi)$ in Fig. 6(b), which also favors the 53° angle. Indeed $\beta(\psi)$ vanishes for this value of ψ, indicating that the eight sets of wave vectors like $(\overrightarrow{OA_1},\overrightarrow{OA_2})$ are not coupled, and may coexist on the first ring. On the contrary the large value of the coupling coefficient between orthogonal vectors, $\beta(\psi)\approx 2.4$, prevents the quasiperiodic pattern formation, [the coupling between vectors $(\overrightarrow{OA_2},\overrightarrow{OB_1})$ is also strong, but its contribution is twice smaller for the present (8-8) pattern than for a quasipattern].

B. (8-12) pattern

With the flat filter $R_1(K)$ the (4-4) pattern also destabilizes near $r\approx 1.7$. leading to the (8-12) pattern show in Figs. 9. From the onset the near field has lost the reflection symmetry, while it is spatially periodic, as the (8-8) pattern, but

greatly differs [Fig. 9(a) and 9(b)]. The spectrum, symmetrical with respect to the two axis [Fig. 9(c) and 9(d)], displays the same peaks as the (8-8) pattern described above, plus four E_i peaks on the second ring, which are the brightest ones.

At $E_0=0.022$ the time trace is constant over thousands of round trip times, the spectrum displays two sets of bisquares twisted by 53°, with equal amplitudes ($A_i\approx 0.15$, $C_i=0.05$) on the first and second ring, respectively, plus the four bright E_i peaks with amplitude 0.15.

At $E_0=0.023$, a very tiny increment is observed on the time trace after a very long integration time. In the near field the pattern is still periodic, but in the far field there is no more equipartition of the energy in the first set of modes. The two rectangles joined by the solid lines in Fig. 9(d) become brighter ($A_i=0.25$, $C_i=0.1$), the others get darker ($A_i=0.1$, $C_i=0.04$). In that case the far field mainly consists in three rhombuses, but their vertex angles forbid any resonant coupling between modes $(K,K'_{\pm})$, while the resonant $(K,\sqrt{2}K)$ coupling persists between the two orthogonal rhombuses of the first ring. While this pattern formation is not well understood, let us notice that it also results from a mode-locking process, since the vectorial mode-locking relations, Eqs. (51), still exist, moreover the growth of the E_i peaks occurs because $\overrightarrow{E'_1E_2}=\overrightarrow{B'_2B_1}$.

In summary these patterns illustrate a case of secondary bifurcation where two twisted patterns are formed from an original structure. The original (4-4) structure is here not destroyed, similarly to the case analyzed by Müller in terms of weak $(K,2K)$ coupling.

But the final (8-8) or (8-12) arrangements are different, since the peaks are not regularly distributed in our case. Moreover, the twisting angle 53° does not result from a triadic interaction between critical wave vectors (K,K') as in Müller's case, but it results from the vectorial relations, Eqs. (50), that allows a spatial mode locking with basic wave vectors $\vec{K}_{\text{lock1,2}}$. Now let us return to the ''rotated'' straight pattern described in Sec. II A, and use the notations of Fig. 2(d) and 8(e) to describe the location of the peak intensity in the far field of Figs. 2 and 3, with (A_0,B_0,C_0,D_0) for the straight pattern, and (A_2,B_2,C_2,D_2) for the rotated one. Curiously $\vec{K}_{\text{lock}}$ is also equal to the drift vector A_0A_1 responsible for the rotation of the first ''straight'' structure, therefore the $\vec{k}_{\text{lock}}$ modes which emerge near $r\approx 1.8$ were responsible for the rotation at $r\approx 1.43$.

V. CIRCULAR INPUT BEAM

While one expects a continuous transition between results using the plane-wave approach, and those of a finite-size beam, the patterns obtained in the defocusing side of the resonance are boundary dependent up to very large aspect ratios. This result can be supported by an estimation of the boundary effects in Eq. (10). Let us suppose now that $E=E_s(\mathbf{r})(1+A)$, where $E_s(\mathbf{r})$ is the stationary profile for a circular input beam $E_0(\mathbf{r})$. The perturbation E_sA obeys the equation

$$\partial_{t'}E_s(\mathbf{r})A(\vec{r},t)=-E_s(\mathbf{r})A(\vec{\mathbf{r}},t)+i\,\eta r E_s(\mathbf{r})(2A+A^*+A^2+2|A|^2+A|A|^2)+a\left\{\exp i\left(\frac{L}{2k}\,\nabla_T^2\eta\theta_{cav}\right)-1\right\}E_s(\mathbf{r})A(\vec{\mathbf{r}},t). \tag{51}$$

In the case of a Gaussian input profile, let us set $E_s(\mathbf{r})=E_s\exp(-\mathbf{r}^2/w^2)$ and $A(\vec{\mathbf{r}})=A\exp(iK_0x)$, with $\mathbf{r}^2=x^2+y^2$. The effect of the free-space propagation in the cavity, which appears in the last term of Eq. (51) may be written as

$$\left\{\exp i\frac{L}{2k}\,\nabla_T^2-1\right\}E_s(\mathbf{r})A(\vec{\mathbf{r}})=\{\exp(-i\,\theta_c+\beta)-1\}\times E_s(\mathbf{r})A(\vec{\mathbf{r}}), \tag{52}$$

with $\theta_c=\theta(K_c)$ [Eq. (4)], and

$$\beta=\frac{2K_cLx}{kw^2}-\left(\frac{K_cL}{kw}\right)2+2i\,\frac{Lx^2}{kw^4}. \tag{53}$$

In the beam waist, for $x\approx w$, one has $\beta\approx(2K_0L/kw)$. The condition for Eq. (51) to reduce to Eq. (11) is $\beta\ll|\sin\theta_c|$, else in terms of the aspect ratio $\Gamma=K_cw/\pi$.

$$\Gamma\gg\frac{4}{\pi}\,\frac{\theta_c}{|\sin\theta_c|}. \tag{54}$$

At threshold the diffraction parameter correspond $\theta_c=0.2$, and 6.1 for the focusing and defocusing case, respectively, ($\sin\theta_c=-0.2$), that gives

$$\Gamma\gg 1 \quad \text{in the focusing case,} \tag{55}$$

$$\Gamma\gg 40 \quad \text{in the defocusing case.} \tag{56}$$

Therefore the plane-wave limit is expected to be valid for very large aspect ratios in the defocusing side.

Let us now describe the numerical results obtained either with a Gaussian input, and aspect ratios increasing from $\Gamma\approx 10$ up to $\Gamma\approx 20$, or with a flat circular input with aspect ratios up to $\Gamma\approx 35$. For these simulations a 384×384 grid was used. We have no results for larger values of Γ.

(a) With a Gaussian input amplitude E_0, for $\Gamma\approx 10$, the stationary profile is bell-shaped over a large range of control parameter, until $E_{0,\text{hex}}=5E_{0,th}$ where it destabilizes into an hexagonal structure [2]. For $\Gamma\approx 20$, the top of the bell-shaped profile gets rings at $E_0=2.8E_{0,th}$, then the inner rings get modulations; and the hexagonal structure appears at $E_{0,\text{hex}}=4E_{0,th}$. For aspect ratio $\Gamma\approx 20$, the patterns obtained below $E_{0,\text{hex}}$ are therefore similar to the ones obtained in the focusing case with aspect ratio of order unity, leading to the daisylike structures [11].

(b) With a flat circular input, the profile gets concentric rings below the linear plane-wave threshold, even for an aspect ratio of order ten, and they persist above the threshold. When increasing E_0, the rings become slightly modulated as shown in Fig. 10, and finally large hexagonal modulations are observed. As in the Gaussian input case, the threshold for

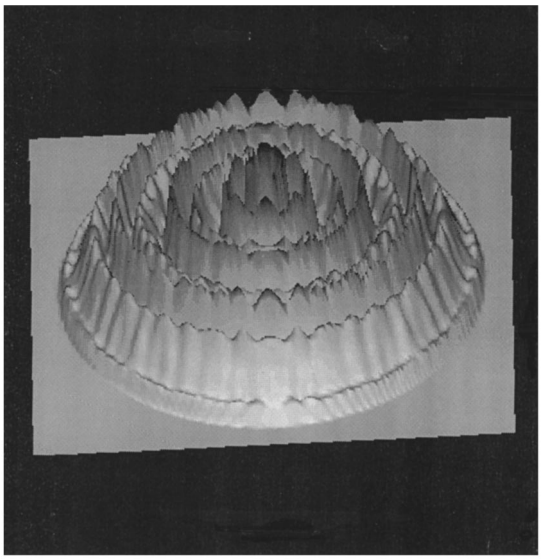

FIG. 10. With a flat circular input $\Gamma=10$ the concentric rings observed on the near-field intensity profile (from $E_0=0.006$, up to 0.060) get small modulations above the threshold ($E_{0,th}=0.012$). Here $E_0=0.025$.

the appearance of hexagons decrease when increasing the aspect ratio ($E_{0,\mathrm{hex}}\approx 5E_{0,th}$ for $\Gamma\approx 10$; while $E_{0,\mathrm{hex}}\approx 2.4E_{0,th}$ for $\Gamma\approx 35$).

These numerical results agree with the prediction of the finite-size effects for aspect ratios as large as 35. The role of the boundary is to favor the rings at the first bifurcation. The spectral components for the second, third, etc., cones are present on the form of concentric rings in the far field, but they are much weaker than the first ring. Thus the boundary seems to raise the outer cone thresholds, that may explain the appearance of hexagons at the secondary bifurcation. Finally the observation of bi-square with a circular input beam should require very large aspect ratios, due to relation (56). Such important effects due to the boundary conditions were absent in the focusing case, in agreement with relation (55), and also in the study of polarization instability of the feedback-mirror device [5] where $(\theta_c/|\sin\theta_c|)\approx 1$ on both side of the resonance.

VI. CONCLUSION

Multiconical emission of light was also observed after propagation through a nonlinear medium [18], without any cavity. This process was understood in the case of a thin nonlinear medium, as an interference effect in the far field between two parts of the phase-encoded beam profile. Such effect appears if the intensity of the input varies along the transverse profile, consequently it cannot be observed with a plane-wave input. While in the ring cavity case, the multiconical emission is predicted and numerically observed either with a finite-size beam or with a plane-wave input with periodic boundary conditions.

In summary with a plane-wave input beam, the pattern formation results from a strong intermode coupling, differently from the Müller model. Indeed the monoconical hexagonal structure is never obtained with a plane-wave input beam, the emerging structure being a bisquare at threshold. Then the bisquare structure destabilizes into the mode-locked structures of Figs. 8 and 9, which keep the ''memory'' of the biconical one, splitting into two twisted biconical structures.

The secondary bifurcation leading to the ''rotated'' (4-4) structure, was interpreted as a drift bifurcation while no drifting solution was observed. On the contrary, after destabilization of the latter structure we have observed (8-8,12) patterns that clearly display unlocked phases and drift very slowly on a small range of critical parameters.

ACKNOWLEDGMENTS

The numerical simulations have been realized with the Cray C98 of the IDRIS CNRS computer center. The authors greatly acknowledge fruitful discussions with T. Erneux, P. Mandel, S. Fauve, and P. Manneville.

APPENDIX A: AMPLITUDE EQUATIONS FOR THE BISQUARE WITH ∂_t, $\mu\approx\epsilon$

The second-order equation (22) is still valid with a right-hand side (f_2,g_2) given by Eq. (23) plus the additional term $(1,c)^t\partial_1 R_1$. The solvability conditions are then

$$\frac{2\eta c}{(3-c^2)}\,\partial_1 R_1 = r_1 R_1 + 2r_{cr}(R_1 R_1')_r, \tag{A1}$$

$$\frac{2\eta c'}{(3-c'^2)}\,\partial_1 R_1 = r_1' R_1' - 2r_{cr}\gamma'(R_1^2)_r. \tag{A2}$$

A particular solution of second-order equation, orthogonal to the kernel of the adjoint operator is

$$\mathbf{A}_2 = u(1-ic)(R_1R_1')_r + v(1-ic)r_1R_1 + u'(1-ic')(R_1'^2)_r + v'(1-ic')r_1'R_1' + (|A_1^2|+|B_1^2|)g + (|C_1^2|+|D_1^2|)g' \tag{A3}$$

with the same notations as in Eq. (26), and

$$w = -\eta r_{cr}\left(\frac{3}{2c}+\frac{c}{2}+c'\right);\quad w' = -\eta r_{cr}'\left(\frac{3}{c'}+2c+\frac{c^2}{c'}\right);$$

$$v = -\frac{\eta}{2}\left(\frac{3-c^2}{2c}+c\right);\quad v' = -\frac{\eta}{2}\left(\frac{3-c'^2}{2c'}+c'\right).$$

At third order, the solvability condition are

$$r_2R_1 + \frac{3+c^2}{3-c^2}\,r_1(R_2)_r - 2r_1(R_1R_1')_r - r_cZ = 0, \tag{A4}$$

$$r_2'R_1' + \frac{3+c'^2}{3-c'^2}\,r_1'(R_2')_r - 2r_1'(R_1^2)_r' - r_c'Z' = 0, \tag{A5}$$

where

$$Z = W + \left(2r_1'v' + \frac{f}{u}\,r_1v\right)(R_1R_1')_r, \tag{A6}$$

$$Z' = W' + 2r_1v(R_1^2)_{r'}. \tag{A7}$$

A combination of the second- and third-order solvability conditions, respectively, multiplied by ϵ^2 and ϵ^3 leads to the following system of coupled equations:

$$\partial_t A=\mu(1+m\mu)A+\beta_A AC+A(\delta A^2+\sigma C^2), \quad \text{(A8)}$$

$$\zeta\partial_t C=\mu'(1+m'\mu')C+\beta_C A^2+C(\delta' C^2+\sigma' A^2), \quad \text{(A9)}$$

with

$$\beta_A=2_\gamma+\mu 1_1+1_{12\mu'};\beta_C=-2\gamma'+\mu' 1_2+1_{21\mu}, \quad \text{(A10)}$$

$$m=\frac{3+c^2}{3-c^2}\,v r_{cr},\ \ m'=\frac{3+c'^2}{3-c'^2}\,v' r'_{cr}; \quad \text{(A11)}$$

$$1_1=2\left(2_\gamma+r_{cr}v\frac{f}{u}\right),\ \ 1_{12}=2r'_{cr}v'\,\frac{f}{u},\quad 1_2=-2\lambda_{\gamma'},$$

$$1_{21}=2r_{cr}v\,\frac{e'}{u} \quad \text{(A12)}$$

and δ, σ, δ', σ' are given in Eqs. (37).

APPENDIX B: ANGULAR COUPLING FOR TWO SETS OF ACTIVE MODES

The weakly nonlinear analysis of the biconical pattern is presented in the text, Sec. III C, within the hypothesis of orthogonal wave vectors on each cone. Here we generalize the calculation to a (4-4) pattern with arbitrary vertex angle $\Psi=(\vec{K}_i,\vec{K}_j)$. Let us write

$$R_1=A_i e^{i\vec{K}_i\vec{x}}+A_j e^{i\vec{k}_j\vec{x}}+\text{c.c.}, \quad \text{(B1)}$$

$$R'_1=C_1 e^{i(\vec{k}_i+\vec{K}_j)\vec{x}}+D_1 e^{i(\vec{K}_i-\vec{K}_j)\vec{x}}+\text{c.c.} \quad \text{(B2)}$$

The two sets of active modes with wave numbers $K_c=|\vec{K}_i|=|\vec{K}_j|$ and $K'_\pm=|\vec{K}_i\pm\vec{K}_j|$, become linearly unstable at $[r_{cr},\ \Theta=\text{a sin}\,\theta(K)]$ and $[r'_{cr\pm},\ \Theta'_\pm=a\ \sin\Theta(K'_\pm)]$, respectively, with $\theta_\pm$ given by

$$\theta_\pm=\theta(K'_\pm)=2\,\theta(K)(1\pm\cos\,\psi) \quad \text{(B3)}$$

With these three distinct threshold values, the derivation of the amplitude equations for the biconical nonorthogonal structure is a straightforward generalization of the orthogonal mode case. The only difference lies in the fact that the modes $K'_\pm$ have two different thresholds, it results that all the coefficients depending on $(c',\gamma',e,e',\ldots)$, in Sec. III C, split into $(c'_\pm,e_\pm,\gamma'_\pm)$, with

$$c'_\pm=-\Theta'_\pm+3r'_{cr\pm} \quad \text{(B4)}$$

deduced from Eqs. (21).

At first order the imaginary part of the order parameter $\mathbf{A}_1$ is

$$I_1+I'_1=cR_1+c'_+R'_{1+}+c'_-R'_{1-}+\text{c.c.} \quad \text{(B5)}$$

At second order Eq. (22) leads to the system

$$r_1R_1=r_c\gamma[(R_1R'_{1+})_r+(R_1R'_{1-})_r], \quad \text{(B6)}$$

$$r'_{1\pm}R'_{1\pm}=-r'_{c\pm}\gamma'_\pm(R_1^2)_{r'}. \quad \text{(B7)}$$

Particular solutions of the second-order equation [Eq. (22)] are similar to Eqs. (26), with $u'\to u'_\pm, g'\to g'_\pm$, and finally the third-order solvability condition is similar to Eqs. (30). The relevant term for our purpose is W, which contains the self-coupling A_i,A_i and the intermode coupling A_i,A_j. Let us note $W_{\vec{A}i}$ the part of W relative to the Fourier component $\exp(i\vec{K}_i\vec{x})$. The generalization of Eq. (30) gives

$$W_{A_i}=A_i[(2g+3j)|A_i^2|+a_{ij}|A_j^2|+a_+|C_1^2|+a_-|D_1^2|]$$
$$+aA_i^*C_1D_1, \quad \text{(B8)}$$

where $a_{ij}=2g+2(e_++e_{\vec{-}})+6j$. The coupling coefficient between the two modes $(\vec{K}_i,\vec{K}_j)$ is then

$$\beta(\psi)=\frac{a_{ij}}{2g+3j}=1+\frac{1}{2g+3j}\,[2(e_++e_-)+3j], \quad \text{(B9)}$$

with

$$e_\pm=-\eta r'_\pm\left(c'_\pm\,\frac{3+c^2-2cc'_\pm}{c'^2_\pm-3}+2c\right). \quad \text{(B10)}$$

APPENDIX C: ANGULAR COUPLING FOR A MONOCONICAL PATTERN

The weakly nonlinear analysis of Eq. (10) solutions in the vicinity of the threshold is detailed here when monoconical emission occurs. This problem was treated in the case of critical wave number K_{th} [2,8,9]; here we generalize the calculation for arbitrary value K_c in the vicinity of K_{th}, with the notations of Sec. III B.

1. Hexagonal structure

In the case $\Psi=\pi/3$, the quadratic nonlinearity leads to resonant terms at second order, as in the biconical case. The amplitude equations are derived with the same scalings as in Sec. III B.

At first order the complex field amplitude has real and imaginary parts

$$R_1=A_1e^{i\vec{K}_i\vec{x}}+B_1e^{i\vec{K}_j\vec{x}}+C_1e^{i\vec{K}_m\vec{x}}+\text{c.c.} \quad \text{(C1)}$$

$$I_1=cR_1,$$

where $\vec{K}_{i,j,m}$ are three wave vectors with vertex angles $\pi/3$, and equal moduli K which become linearly unstable at r_{cr} given by Eq. (13)

At second order, Eq. (22) with

$$\begin{pmatrix} f2\\ g2\end{pmatrix}=\begin{pmatrix} c\\ -3\end{pmatrix}\eta r_1R_1+\eta r_{cr}\begin{pmatrix} 2cR_1^2\\ -(3+c^2)R_1^2\end{pmatrix} \quad \text{(C2)}$$

leads to the solvability condition $cf_2+g_2=0$ or

$$r_1R_1=-r_{cr}(R_1^2)_r \quad \text{(C3)}$$

and the particular solution which is orthogonal to the kernel of $\mathbf{L}^+$ is of the form

$$R_2=\alpha_0(R_1^2)_0+\alpha_1(R_1^2)_K+\alpha_3(R_1^2)_{\sqrt{3}_K}+\alpha_4(R_1^2)_{2K}, \quad \text{(C4)}$$

$$I_2=\beta_0(R_1^2)_0+\beta_1(R_1^2)_K+\beta_3(R_1^2)_{\sqrt{3}_K}+\beta_4(R_1^2)_{2K}, \quad \text{(C5)}$$

where the index $_{\sqrt{n}K}$ in (R_1^2) is relative to the modulus of the wave vector, and

$$\alpha_1=\eta c r_{cr}/2, \quad \beta_1=-c\alpha_1, \quad \text{(C6)}$$

$$\alpha_n=\frac{f_2(n)+b(n)g_2(n)}{b(n)c(n)-1}, \quad \beta_n=\frac{c(n)f_2(n)+g_2(n)}{b(n)c(n)-1}, \quad \text{for } n\neq 1 \quad \text{(C7)}$$

with $\Theta_n=R/(1-R)\sin(nK^2+\eta\theta_{cav})$ and

$$b(n)=\Theta_n-\eta r_{cr}, \quad c(n)=3\eta r_{cr}-\Theta_n. \quad \text{(C8)}$$

At third order the solvability condition is

$$\frac{2\eta c}{(3-c^2)}\partial_2 R_1=r_2R_1+r_1\frac{3+c^2}{3-c^2}(R_2)_r+r_{cr}\sqrt{R_1R_{2r}}+(1-c)\frac{1+c^2}{3-c^2}(R_1^3)_r+r_1(R_1^2)_r. \quad \text{(C9)}$$

The addition of the two solvability conditions (C2)–(C5) multiplied by ϵ^2 and ϵ^3 respectively, leads to the coupled set of amplitude equations for $A=\epsilon A_1$, $B=\epsilon B_1$, $C=\epsilon C_1$,

$$\partial_\tau A=\mu A+(1+l\mu)BC+A[e|A^2|+f(|B^2|+|C^2|], \quad \text{(C10)}$$

where

$$e=2\alpha_0+\alpha_4+3j, \quad f=2\alpha_0+\alpha_1+\alpha_3+4j. \quad \text{(C11)}$$

$$l=\frac{3+c^2}{3-c^2}\alpha_1, \quad j=\frac{(1-c)(1+c^2)}{3-c^2} \quad \text{(C12)}$$

The coupling function defined in Eq. (47) appears in Eqs. (C10) as

$$\beta(\pi/3)=\frac{f}{e}. \quad \text{(C13)}$$

For a tuned cavity ($\theta_{\text{cav}}=0$) and $K=K_{th}$, the value $\beta(\pi/3)=0.77$ is reported in dots in Fig. 6(b).

2. Two modes with vertex angle $\Psi\neq\pi/3$

In the case of two modes with amplitudes $A=\epsilon A_1+\epsilon^2A_2$, $B=\epsilon B_1+\epsilon^2B_2$, and arbitrary value of $\Psi\neq\pi/3$, the first-order expansion for the field is of the form

$$R_1=A_1e^{i\vec{K}\vec{i}\vec{x}}+B_1e^{i\vec{K}\vec{j}\vec{x}}+\text{c.c.}$$

$$I_1=cR_1. \quad \text{(C14)}$$

Since the quadratic term in the second order Eq. (C2) is nonresonant, the solvability condition [Eq. (C3)], is

$$r_1=0, \quad \text{(C15)}$$

and the particular solution

$$R_2=\alpha_0(R_1^2)_0+\alpha_+(R_1^2)_{K+}+\alpha_-(R_1^2)_{K-}+\alpha_4(R_1^2)_{2K}, \quad \text{(C16)}$$

where α_0 is given in Eq. (A7) and (A8) and $\alpha_\pm$ is like α_n with

$$n\rightarrow\phi_\pm=2(1\pm\cos\Psi). \quad \text{(C17)}$$

In the case of critical wave number $K_c=K_{th}$,

$$\alpha_0=-\frac{3-2\theta}{(\theta-2)^2}; \quad \alpha_\pm=2\frac{2\theta-3+2\phi_\pm(2-\theta)}{(2-\theta)^2(1-\phi_\pm^2)}. \quad \text{(C18)}$$

At third order, the solvability condition, Eq. (C9) where $r_1=0$, leads to the amplitude equation,

$$\partial_\tau A=\mu A+A[e|A^2|+f|B^2|] \quad \text{(C19)}$$

and symmetrical relation for $\partial_\tau B$, where e is given by Eq. (C13) and

$$f=2\alpha_0+\alpha_++\alpha_-+4j. \quad \text{(C20)}$$

The coupling function between the A, B modes appearing in Eq. (C19),

$$\beta(\Psi)=\frac{f}{e} \quad \text{(C21)}$$

is drawn on Fig. 6(b) for the tuned cavity with critical wave number K_{th}.

[1] A. S. Patrascu, C. Nath, M. Le Berre, E. Ressayre, and A. Tallet, Opt. Commun. **91**, 433 (1992).

[2] M. Le Berre, S. Patrascu, E. Ressayre, A. Tallet, and N. I. Zheleznykh, Chaos Solitons Fractals **4**, 1389 (1994).

[3] G. D'Alessandro and W. J. Firth, Phys. Rev. A **46**, 537 (1992); M. A. Vorontsov, N. G. Iroshnikov, and R. L. Abernathy, Chaos Solitons Fractals **4**, 1701 (1994).

[4] J. B. Geddes, R. A. Indik, J. V. Moloney, and W. J. Firth, Phys. Rev. A **50**, 3471 (1994); J. B. Geddes, J. Lega, J. V. Moloney, R. A. Indik, E. M. Wright, and W. J. Firth, Chaos Solitons Fractals **4**, 1261 (1994).

[5] D. Leduc, M. Le Berre, E. Ressayre, and A. Tallet, Phys. Rev. A **53**, 1072 (1996); (unpublished).

[6] E. Pampaloni, P. L. Ramazza, S. Residori, and F. T. Arecchi, Phys. Rev. Lett. **74**, 258 (1995); E. V. Degtiarev and M. A. Vorontsov, J. Mod. Opt. **43**, 93 (1996).

[7] H. W. Müller, Phys. Rev. E **49**, 1273 (1994).

[8] W. J. Firth, A. J. Scroggie, G. S. McDonald, and L. A. Lugiato, Phys. Rev. A **46**, R3609 (1992); A. J. Scroggie, W. J. Firth, G. S. McDonald, M. Tlidi, R. Lefever, and L. A. Lugiato, Chaos Solitons Fractals **4**, 1323 (1994).

[9] M. Tlidli, Ph.D. thesis, Université Libre de Bruxelles, Bel-

gique, 1995; M. Tlidli, R. Lefever, and P. Mandel (unpublished).
[10] K. Ikeda, Opt. Commun. **30**, 257 (1979).
[11] M. Le Berre, S. Patrascu, E. Ressayre, and A. Tallet, Opt. Commun. **123**, 810 (1996).
[12] L. A. Lugiato and R. Lefever, Phys. Rev. Lett. **58**, 2209 (1987); L. A. Lugiato and C. Oldano, Phys. Rev. A **37**, 3896 (1988).
[13] P. Manneville, *Dissipative Structures and Weak Turbulence* (Academic, New York, 1990).
[14] G. Dangelmayr, Dyn. Stab. Syst. **1**, 159 (1986).
[15] D. Armbruster, J. Guckenheimer, and P. Holmes, Physica D **29**, 257 (1988).
[16] M. R. E. Proctor and C. Jones, J. Fluid Mech. **188**, 3011 (1988).
[17] S. Fauve, S. Douady, and O. Thual, J. Phys. (France) II **1**, 311 (1991).
[18] S. D. Durbin, S. M. Arakelian, and Y. R. Shen, Opt. Lett. **6**, 511 (1981); see also M. Le Berre, E. Ressayre, and A. Tallet, Phys. Rev. A **25**, 1604 (1982); M. Le Berre, E. Ressayre, A. Tallet, K. Tai, H. M. Gibbs, M. C. Rushford, and N. Peyghambarian, J. Opt. Soc. Am. B **1**, 591 (1984). See also the recent experiment by E. T. T. Nibbering, P. F. Curley, G. Grillon, B. F. Prade, M. A. Franco, F. Salin, and A. Mysyrowicz, Opt. Lett. (to be published).